Electronic Supplementary Material (ESI) for Materials Horizons.
This journal is © The Royal Society of Chemistry 2020

# Supporting Information

## A highly selective electron affinity facilitated $H_2S$ sensor: the marriage of tris(keto-hydrazone) and organic field-effect transistor

Saravanan Yuvaraja,[a□] Veerabhadraswamy Nagarajappa Bhyranalyar,[b□] Sachin Ashok Bhat,[b]
Sandeep Goud Surya,[*a] Channabasaveshwar Veerappa Yelamaggad,[*b] Khaled Nabil Salama[*a]

[a]Sensors lab, Advanced Membranes and Porous Materials Center,
Computer, Electrical and Mathematical Science and Engineering Division,
King Abdullah University of Science and Technology (KAUST),
Thuwal, 23955-6900, Kingdom of Saudi Arabia
E-mail: (sandeep.surya@kaust.edu.sa, khaled.salama@kaust.edu.sa)

[b]Centre for Nano and Soft Matter Sciences (CeNS),
Jalahalli, Bengaluru 560 013, India.
E-mail: (yelamaggad@cens.res.in)

[□] Saravanan Yuvaraja and Veerabhadraswamy Nagarajappa Bhyranalyar have contributed equally.

Table of contents

## Experimental section

***Synthesis and characterization of tris(keto-hydrazone)s***: To a well-stirred and cooled (-5 $^{o}$C) solution comprising 4-aminophenyl 3,4,5-tris(heptyloxy)benzoate (0.48 mmol, 3 eq.) in 1:1 mixture of THF-methanol and 3 ml of a 2M HCl, a solution of $NaNO_2$ (0.02g, 0.32 mmol, 2 eq.) in 3 ml of water was added drop-wise slowly. The reaction mixture was allowed to warm-up to room temperature to which a solution of phloro glucinol (0.02g, 0.159 mmol, 1 eq.) in methanol / 2M NaOH was added drop-wise. The reaction mixture was stirred for 30 mins. The pH of the reaction mixture was neutralized with diluted HCl, and the resultant mixture was poured into the water, and extracted with dichloromethane (3 × 30ml). The crude product was purified using column chromatography using neutral alumina. Initially, the column was eluted with hexanes, followed by 20% EtOAc-hexanes to obtain the desired compound. This was further purified by recrystallization using absolute ethanol.

***HDN4 (M2):***A wine red solid; yield: 119.6 mg (52%); FTIR (KBr pellet): $\nu_{max}$ in cm$^{-1}$ 3453, 2958, 2874, 1738, 1588, 1480, 1429, 1332 and 1176; UV-Vis: $\lambda_{max}$ = 497.9 nm (absorption) and 575 nm (emission), ε = 7.53 × $10^2$ L $mol^{-1}$ $cm^{-1}$; $^1H$ NMR (400MHz, $CDCl_3$) : δ 16.43 ( s, 3H, 3 × NH), 7.72 (d, *J* = 8.4 Hz, 6H, Ar), 7.42 (s, 6H, Ar), 7.34 (d, *J* = 8.4 Hz, 6H, Ar), 4.10 (m, 18 H, 9 × $OCH_2$), 1.85 -0.96 (m, 63 H, 18 × $CH_2$,9 × $CH_3$); $^{13}C$ NMR (100 MHz, $CDCl_3$): 178.65, 164.86, 153.06, 150.20, 143.33, 138.91, 128.94, 123.47, 123.39, 118.62, 108.70, 73.27, 69.04, 32.37, 31.36,19.29, 19.16, 13.88, 13.84; Anal. calcd for $C_{81}H_{102}N_6O_{18}$ : C, 67.20; H, 7.10; N, 5.81.Found: C, 66.98; H, 7.32; N, 5.80. $^1H$ NMR and $^{13}C$ NMR of HDN4 is presented in Fig. S1A and S1B respectively.

***HDN6 (M3)****:* A wine red solid; yield: 143.3 mg (52%); FTIR (KBr pellet): $\nu_{max}$ in $cm^{-1}$ 3434, 2932, 2863, 1734, 1589, 1482, 1429, 1335 and 1175; UV-Vis: $\lambda_{max}$ = 497.3 nm (absorption) and 575 nm (emission), ε = 2.80 × $10^2$ L $mol^{-1}$ $cm^{-1}$; $^1H$ NMR (400MHz, $CDCl_3$) : δ 16.42 ( s, 3H, 3 × NH), 7.72 (d, *J* = 8.4 Hz, 6H, Ar), 7.41 (s, 6H, Ar), 7.34 (d, *J* = 8.4 Hz, 6H, Ar), 4.09 (m, 18 H, 9 × $OCH_2$), 1.87 -0.90 (m, 99 H, 36 × $CH_2$,9 × $CH_3$); $^{13}C$ NMR (100 MHz, $CDCl_3$): 178.65, 164.86, 153.05, 150.20, 143.33, 138.91, 128.94, 123.46, 123.39, 118.61, 108.70, 73.64, 69.36, 31.74, 31.57, 30.32, 29.29, 25.77, 25.72, 22.69, 22.63, 14.08, 14.03; Anal. calcd for $C_{99}H_{138}N_6O_{18}$ : C, 69.94; H, 8.18; N, 4.94.Found: C, 70.11; H, 8.34; N, 5.02. $^1H$ NMR and $^{13}C$ NMR of HDN6 is presented in Fig. S2A and S2B respectively.

***HDN7 (M4)****:* A wine red solid: Heating: Cr 82.5 (1 kJ/mol) $Col_{r2}$ 154.9 (0.4) $Col_{r1}$ 183 (4.1) I; Cooling: I 178.1 (3.8) $Col_{r1}$ 148.2 (0.2) $Col_{r2}$; yield: 145.2 mg (49%); FTIR (KBr pellet): $\nu_{max}$in $cm^{-1}$ 3484, 2928, 2856, 1734, 1588, 1482, 1429, 1335 and 1175; UV-Vis: $\lambda_{max}$ = 498.2 nm (absorption) and 578 nm (emission), ε = 6.35 × $10^2$ L $mol^{-1}$ $cm^{-1}$; $^1H$ NMR (400MHz, $CDCl_3$) : δ 16.43 ( s, 3H, 3 × NH), 7.72 (d, *J* = 8.4 Hz, 6H, Ar), 7.41 (s, 6H, Ar), 7.34 (d, *J* = 8.4 Hz, 6H, Ar), 4.09 (m, 18 H, 9 × $OCH_2$), 1.84 -0.88 (m, 117 H, 45 × $CH_2$,9 × $CH_3$); $^{13}C$ NMR (100 MHz, $CDCl_3$): 178.65, 164.86, 153.05, 150.20, 143.34, 138.91, 128.94, 123.45, 123.39, 118.61, 108.71, 73.64, 69.36, 31.93, 31.83, 30.37, 29.34, 29.23, 29.07, 26.06, 26.02, 22.68, 22.63, 14.11, 14.09; Anal. calcd for $C_{108}H_{156}N_6O_{18}$ : C, 71.02; H, 8.61; N, 4.60.Found: C, 70.69; H, 8.77; N, 4.60. $^1$H NMR and $^{13}$C NMR of HDN7 is presented in Fig. S3A and S3B respectively.

The tris(keto-hydrazone)s, namely, **HDN4** (**M2**), **HDN6** (**M3**) and **HDN7** (**M4**), designed and synthesized here are a novel class of $C_3$-symmetric, (n, π-conjugated) functional organic compounds (**Ia / Ib**) possessing a central cyclohexane-1,3,5-trione ring where three-keto groups are substituted alternatively on a cyclohexane ring. These compounds are stabilized by the resonance-assisted intramolecular H (hydrogen)-bonding. In fact, they are tautomers of tris(azo-enol)s (**Ic**). These materials, prepared by a triple azo coupling reaction between anilines and phloroglucinol, were found to exist in tris(keto-hydrazone) $C_{3h}$ (**Ia**) form but not in Cs (**Ib**) form / tris(azo-enol)s (**Ic**) state. This finding has been evidenced unequivocally with the aid of NMR spectroscopic data. Figures S4a and S4b respectively depict the $^1$H and $^{13}$C NMR spectra recorded in $CDCl_3$ at room temperature for **HDN6**. Other materials show an identical spectral pattern. Importantly, the analysis of these spectra reveals that the compounds, **HDN4** (**M2**), **HDN6 (M3)** and **HDN7** (**M4**), synthesized exist in tris(keto-hydrazone) tautomeric (**Ia**) form having three-fold ($C_{3h}$) rotational symmetry.

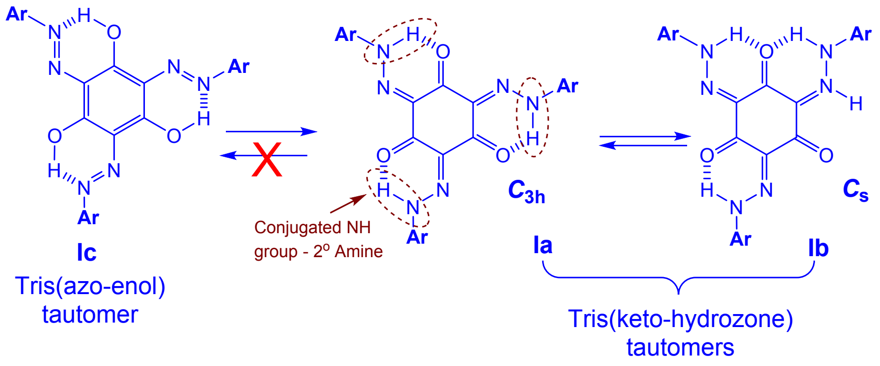

The $^1$H spectrum shows a sharp singlet at ~ 16.5 ppm (see the circle in Fig. S4a) due to the resonance of three protons of three –NH- groups located around the central core. The appearance of N-H proton at the notably low fields suggests the participation of –NH- protons in the intramolecular H-bonding. The $^{13}$C NMR spectrum substantiated the conclusion that the mesogens exist in $C_3$h-tris(keto-hydrozone) (Ia) form. As can be seen in the $^{13}$C spectrum (circle in Fig. S4b), a sharp carbon signal resonating at ~ 178.5 ppm can be assigned to carbonyl carbon (=C=O) of tris(keto-hydrazone) (**Ia**) structure rather than phenolic (=CH-OH) carbon of tris(azo) tautomeric form. Indeed, these NMR data agree with that reported by Lee et al.[1], for analogous materials. Given the fact that compounds **HDN4** (**M2**), **HDN6** (**M3**), and **HDN7** (**M4**) exist in the tris(keto-hydrazone)s (**Ia**) form, their basicity will be relatively high. These forms are quite stable, meaning that they do not undergo tautomerization to yield tris(azo-enol)s (**Ic**). The lone pair of electrons of the NH (2° amine group) do not participate in resonance, and thus, the basicity of the NH group is high. This postulation was substantiated with the help of theoretical studies.

***Sensor fabrication***: A highly doped ($n^{++}$) silicon wafer purchased from the industry and used as a substrate to fabricate bottom-gate bottom-contact (BGBC) organic field-effect transistor (OFET) devices. Initially, the procured silicon wafers were sequentially cleaned in the cleanroom environment using the standard piranha recipe and buffer oxide etchant (buffered HF solution) to remove the native oxide layer. Without any further delay, the cleaned silicon wafers were loaded in the thermal growth system to grow a high-quality 150-nm $SiO_2$ layer via a dry oxidation approach on the surface of the Si substrate using a standard recipe. This was followed by the Si/$SiO_2$ wafer being ultrasonically cleaned in acetone and isopropanol (IPA) solvents for 5 min each before being rinsed in distilled (DI) water for a few minutes. We used a hotplate to heat the $N_2$ blown sample at 120 °C in an open environment for 5 min to remove the residual moisture. Using the standard photolithography process, the interdigitated electrodes were patterned on the surface of an Si/$SiO_2$ substrate. During this process, the substrate was uniformly coated with the widely used AZ-5214 positive photoresist using a spin coating technique. The photoresist-coated sample was heated at 110 °C for 2 min. Subsequently, the desired interdigitated electrode pattern was imaged on the surface of a photoresist-coated sample by exposing it to UV light (75 mJ dose for 7 sec) via a mask containing the desired electrode design. The UV-exposed sample was developed in the AZ-726 developer, which is specially recommended for an AZ-5214 resist–coated sample to remove the photo-exposed regions from the sample. It is important to note that we carefully handled and processed the sample only in the yellow-light region during the photolithography process. After the development step, the sample was gradually taken into the white-light area to deposit the Titanium (Ti) and Gold (Au) metals at a thickness of around 10 nm and 100 nm, respectively, using a radio frequency (RF) sputtering instrument. The obtained sample was subjected to an ultra-sonication-guided lift-off process using acetone and IPA to realize the Ti/Au interdigitated source and drain electrodes, with a channel width (W) and length (L) of around 583,605 μm and 10 μm, respectively, on the surface of the $Si/SiO_2$ substrate. The source and drain deposited wafers were diced into individual substrates and used them to fabricate the gas sensors. The diced substrates were ultrasonically cleaned in acetone, IPA and water for 5 min each and then heated at 120 °C to remove the water residues. In addition, the industry-grade PDVT-10 organic semiconductor was acquired from Lumtec, and a 3 mg/mL PDVT-10 solution was prepared by dissolving the PDVT-10 in a Dichlorobenzene (DCB) solvent. The prepared solution was left undisturbed for 24 hours under continuous stirring and heating at 350 rpm and 110 °C to allow the PDVT-10 polymer to dissolve completely in the DCB solvent. After this process, 4 μL of the PDVT-10 (M1) solution were taken using a micropipette and deposited using a spin coating technique onto the surface of the diced substrate[48] to create the PDVT-10 OFET (D1) sensor. The as-synthesized tris(keto-hydrazone)s (M2-M4) were mixed with a chloroform solvent to prepare 5 mg/0.5 mL solution. Before moving further with the tris(keto-hydrazone) deposition process, we were eager to test whether the chosen chloroform solvent can affect the underlying the PDVT-10 layer. To confirm this, primarily, we have characterized the device and the corresponding transfer curve (labeled as "before chloroform") was recorded by sweeping $V_G$ = +20 to -30 V at $V_D$ = -30 V, as can be seen in the above Fig. S6a. To test the impact of chloroform on the device channel material, we have drop cast 4 μL of chloroform solution on the surface of PDVT-10 layer, and subsequently heated the device at 100 °C for 15 min. After heating, we have characterized and recorded the transfer curve (labeled as "after chloroform"), as shown in the above Fig. S6a. By comparing both the transfer curves, we can infer that there is a small decline in drain current with a negligible impact on threshold voltage and subthreshold swing. Hence, we can conclude that the channel layer remains intact with no damage after introducing chloroform in the device stack. Followed by, a 4 μL volume of the M2–M4 solutions were drop-cast on the surface of the PDVT-10–coated substrate and heated at 100 °C for 15 min to allow the complete evaporation of solvents; hence, we fabricated the D2–D4 OFET devices. The cross-section field emission scanning electron microscopy (FESEM) of tris(keto-hydrazone) (VC-413)/PDVT-10 stack on the substrate is presented in Fig. S6 (b,c). From these figures, we can further confirm that the underlying PDVT-10 layer remains undisturbed after depositing tris (keto-hydrazone) layer on top. To achieve reproducible electrical device response and sensing characteristics, the same protocol was followed every time to fabricate each OFET sensor (D1–D4).

***Surface characterization studies***: Surface topography features of M1–M4 materials were explored using field-emission scanning electron microscopy (FESEM), atomic force microscopy (AFM) and Kelvin force probe microscopy (KPFM). While using the FESEM (Zeiss-Merlin) instrument, we maintained electron high tension (EHT) and safe working distance around 5.0 kV and 5.0 mm, respectively. In addition, high-resolution images of the samples (M1–M4) were captured with high precision using the special in-lens detector controlled by either analytical or high-resolution operating mode. We used the AFM dimension-icon (Veeco), operated in tapping mode, to probe the surface roughness and film thickness of samples M1–M4. During the AFM characterization experiment, we optimized some of the crucial parameters, namely, integral gain, proportional gain, amplitude set point and drive amplitude, as 20.40, 4.294, 2.486 nm and 500 mV, respectively, until the trace and retrace profiles overlapped, hence yielding high-quality surface AFM images. Finally, we employed the KPFM technique to obtain the surface potential maps of both PDVT-10 (M1) and tris(keto-hydrazone) compounds (M2-M4). Some of the settings, such as integral gain, proportional gain, amplitude set point, drive amplitude, lift scan height and input P-gain, were optimized to 2.686, 5.00, 3.5 nm, 500 mV, 108.0 nm and 10.00 respectively. The thickness, surface roughness and surface potential values of each material (M1–M4) were obtained by taking the average of the values measured from five different locations.

***Electrical studies***: The transistor performance of the fabricated OFET devices (D1-D4) was tested using Keithley 4200 Semiconductor characterization system (SCS) system. The transfer behavior of all the OFET devices was recorded by sweeping the gate-source voltage ($V_{GS}$) from +10 to -30 V for different drain-source ($V_{DS}$) steps from 0 V to -30 V. Whereas, the output characteristics of all the devices were obtained by sweeping $V_{GS}$ from 0 to -30 V for different $V_{DS}$ steps from 0 V to -30 V. From the extracted characteristics, some of the important transistor parameters such as threshold voltage ($V_{TH}$), subthreshold swing (SS), transconductance ($G_m$), current ratio and charge mobility ($\mu_{Sat}$) are calculated using the information provided in SN3 (Supporting Information).

***Gas sensing experiments***: We have installed a smart gas-set up to test the gas sensing performance of various devices. This set up consists of two mass flow controllers (MFC) and one mass flow meter (MFM) whose operations are controlled by Personal computer (PC) via a LabVIEW program interface. The input side of the MFCs is connected to $N_2$ and testing gas cylinders, whereas the output from the MFM block is connected to the gas testing chamber. The chamber-lid is designed with a small holding feature attached on one side that helps us to plug and play the fabricated OFET devices (D1-D4) for testing purpose and the 4200 SCS probes are connected to another side of the lid. The detailed explanation about the gas set up and its features can be found elsewhere.[49]Taking advantage of the two MFCs and $N_2$ inert diluting gas, we can precisely control the concentration of the toxic gases by maintaining an overall 200 SCCM gas volume flows into the chamber. Similar to electrical studies, with the help of a 4200

SCS system, we have recorded the transfer and output characteristics of all the OFET devices toward different concentrations from 5 ppb to 25 ppm. The transistor parameter values corresponding to different gas concentrations were calculated using the above-discussed parameter extraction equations.

***Stability studies related experiments***: The stability of the sensor was tested against bias stress, relative humidity and ambient stability conditions. To study the effect of bias stress on sensing performance, the device under test was connected to the gas chamber and subjected to the fixed gate and drain bias using a 4200 SCS system. During this study, the current responses from the device before and after gas exposure was recorded every two hours using a SCS system. This study was conducted for a total period of 10 hours. To test the device against humidity experiments, we filled the DI water in the bubbler, partially submerged in the ethylene-glycol filled temperature controller bath, to maintain a constant temperature (in this experiment, 20 °C). By mixing the bubbler containing DI water with different volumes of $N_2$ gas, we were able to successfully control the relative humidity of the gas chamber, from 5% to 90% RH conditions. In addition, we were also able to pass the target toxic gas into the chamber without disturbing the relative humidity environment. This feature enables us to test the effect of different relative humidity conditions on the device’s response to various gas concentrations. A long-term ambient stability experiment was conducted for the device's current response toward the presence and absence of toxic gases. During this experiment, the device was stored in the normal laboratory conditions with neither special encapsulation nor a special environment used. The readings were taken for every five days over a total duration of 150 days. To test the reproducibility, instead of one device, we followed the same protocols to record the results from four devices and the corresponding error bar data is plotted. This is followed by all stability studies.

## SN1: Surface morphology study of gas absorbent layers

Fig. 2a (main text) clearly shows the formation of a uniform and pinhole-free spin-coated M1 layer on the surface of the $SiO_2$/Si substrate. After drop-casting, the M2 material leads to the formation of high-density wide cavities, as witnessed in the main text, Fig. 2b. By increasing the number of peripheral side chains from n-butyloxy (M2) to n-hexyloxy (M3), the width and density of surface cavities are reduced (main text Fig. 2c). Interestingly, the latter M3 material showed the sign of forming desired small porous structures that are absent in the case of former M2 material. We can witness the effect of peripheral side chain lengths on the corresponding structural changes, especially the formation of small pores and its density surface distribution. By tracing this relation, we have further increased the side chains from *n*-hexyloxy (M3) to *n*-heptyloxy (M4), and the corresponding structural changes are observed in the main text, Fig. 2d. This figure proves the formation of densely packed small pores while reducing the width and number of unwanted wide cavities. Therefore, the increase in peripheral chains helps improve the formation of small pores, leading to an increase in the surface area of M4 material. With the help of an optimized spin coating recipe, a uniform and ultrathin M1 organic semiconductor layer with a thickness of around 23 nm is formed, as can be seen in the main text, Fig. 2e. To further probe the change in the size of pores formed on the thin films of hydrazones, the high magnification FESEM version of M2, M3 and M4 are imaged (main text Fig. 2f, g and h). The careful inspection of the pore sizes and their distribution reveals that the increase in the peripheral chain length of hydrazones enables the pore sizes to be scaled down, from 200 nm to less than 100 nm with an increase in density.

## SN2: CPD extraction and work function calculation method

1. HOPG calibration step

The main purpose of this step is to find the work function of the tip ($\Phi_{\text{tip}}$) using the standard highly oriented pyrolytic graphite (HOPG) sample.

$\Phi_{\text{tip}} = e * (CPD) + \Phi_{HOPG}$ (1)

It is well known that, the $\Phi_{HOPG}$ value is around 4.6 eV. By running AFM scans on the surface of HOPG sample using the standard AFM tip, we can able to obtain the relative domain potential maps wherein the mean CPD value is calculated. By feeding the mean CPD and $\Phi_{HOPG}$ values in the above equation (1), the $\Phi_{tip}$ was extracted which is around 4.31 eV. This calibration step was carried out every time, corresponding CPD maps can be seen in figure S9, before running the AFM scans of the desired samples such as M1, M2, M3 and M4 materials in this paper.

2. Material work function calculation

$\Phi_{\text{sample}} = \Phi_{tip} - e * (CPD)$ (2)

The extracted $\Phi_{tip}$ value, from the previous step, can be inserted in the equation (2) to find the work function of the sample ($\Phi_{\text{sample}}$)

Hence, we have used the above 2 steps to confirm that the extracted mean CPD values and work function of each materials were accurate and reliable.

Furthermore, in order to obtain the mean CPD values of the entire film, we have considered 10 different locations on the film surface and their corresponding relative domain potential maps were recorded, as can be seen from figures S10 (M1 material) to S13 (M4 material). From these maps, we have calculated the corresponding mean CPD values and plotted in the figure S13.

In the manuscript, we strongly justified that the observed relation attributed to the steric effects.

## SN3: Transistor parameter extraction of OFET device electrical characteristics

The transistor parameters are calculated using the following equations.

The saturation current equation for the transistor device,

$$I_{\text{DSat}} = \frac{\mu_{sat} * W * C_{ox}}{L} * (V_{GS} - V_{TH})^2$$

Subthreshold swing is to find the amount of voltage supplied to obtain one order increase in current. This parameter was calculated from the transfer curve,

$$\mathrm{SS} = \frac{dV_{GS}}{Log_{10} * I_D}\Big|_{\max}$$

Transconductance is to determine the conductivity of the device. This is obtained from the transfer curve using the below equation,

$$\mathrm{G_m} = \frac{dI_D}{d_{VGS}}\Big| \text{ when device operates in linear region.}$$

Charge carrier mobility can be calculated from the transconductance, oxide capacitance ($C_{ox}$), width (W) and length (L) values of the transistor using the below equation,

$$\mu_{\mathrm{Lin}} = \frac{G_m * L}{W * V_{DS} * C_{ox}} \text{ , device operates in linear regime.}$$

## SN4: Stability studies of OFET $H_2S$ sensor

One of the serious challenges to use organic-based functional materials on the device for sensing toxic gases is they are highly vulnerable to irreversible degradation due to harsh environmental conditions and electrical bias applied for a long time. All the tested devices were suspended in normal lab conditions with no special coating or protections. Primarily, the D4 device was subjected to continuous bias stress, @ $V_{GS} = V_{DS} = -30$ V, over a period of 10 hours. In the $N_2$ atmosphere and absence of target gas, the base current values for every 2 hours were recorded and plotted (main text Fig. 5a(i)). The observed result proves the D4 device experiences a negligible base current drift over the tested period. By following the same testing conditions, we have exposed the D4 device toward 10 ppb and 1 ppm $H_2S$ gas concentrations for every 2 hours and the corresponding current changes were recorded. As can be seen in the main text, Fig. 5a(ii), the D4 device tends to show minimal change in current responses toward both the tested concentrations over a period of 10 hours. Hence, our D4 $H_2S$ OFET sensor is a potential candidate to survive from strong bias stress effects without compromising its sensing performance.

Then, the ambient stability of all the hydrazone based OFET devices (D2-D4) in both the presence and absence of target gas was tested over a period of 150 days. For the D2 device, a sharp decline in the base current of about 50% at the end of 80 days. After this, the device current gradually increased until the end of the testing period reaching around 3.8 µA (Fig. S24). After 1 ppm gas exposure, during the first few days, around 0.96 µA current change witnessed and then a sharp decline in the current levels observed after 80 days (Fig. S24). At the end of 150 days, the difference in current values reached about 0.82 µA. Substantial fluctuations in current levels are observed during both presence and absence of $H_2S$ gas over the entire testing period; hence D2 device does not have good ambient stability. Similarly, the D3 device's ambient stability and its impact on gas sensitivity were also tested (Fig. S25). Unlike D2, the base current of D3 was continuously ramping up with minor fluctuations resulted in observing around 0.9 µA after 150 days, which is around 28.5% higher than the base current observed at day 1. After exposing the D3 device toward 1 ppm $H_2S$ gas, around 1.55 µA and 1.80 µA current change are recorded at the beginning and end of the testing period, respectively. Even-though the fluctuations of current response are reduced, when compared to D2 counterpart, still the stability of the device has to be improved to meet the sensing requirements. The D4 device shows remarkable stability in the base current with negligible fluctuations observed between 7.2 µA and 7.6 µA after testing the device for 150 days (main text Fig. 5b(i)). Whereas, after exposing the D4 device toward 10 ppb and 1 ppm $H_2S$ gas resulted in current changes around 0.96 µA and 4.6 µA respectively, as shown in the main text, Fig. 5b(ii). Moreover, in the entire testing period, no serious fluctuations in the current levels were observed for D4 device. Such high stability of the D4 can be attributed to the amine groups, its dense nature and reduced pore size (< 100 nm) potentially avoiding the interface region from atmospheric moisture and oxygen. The results from stability studies indicate that the D4 device has exhibited less/negligible ambient effects on the gas sensing performance.

The transient response of all the devices (D1-D4) toward 10%, 45% and 90% RH conditions are recorded (Fig. S26). From them, the sensitivity of the devices toward 90% RH alone was calculated and plotted (Fig. S26e). Low sensitivity of device D1 around 20% toward 90% RH aligns with the observation reported in the literature.[2] After adding the hydrazone compounds, unexpectedly, the sensitivity of the D2 device peaked around 80%, which is roughly four times greater than D1 counterpart. Moreover, sensitivity toward 90% RH gradually reduced to approximately 40% and 10% for device D2 and D3, respectively. Negligible sensitivity of the D4 device may attribute to the presence of long peripheral side chains (n-heptyloxy) in M4 material, essentially increases the bulkiness of the thin film. This molecule configuration might increase the surface absorption energy hence retards the interaction of the molecule with the incoming water molecules. The proposed phenomenon can be convincingly attributed to the steric effects of the organic compounds considered as one of the dominant factors to influence the stability of the molecules against humidity conditions.[3] Moreover, relatively thick hydrazone (M4) coating on the surface of M1 possibly impedes the diffusion of water molecules and reducing its possibility to interfere with the dominant hole charges in charge conducting layer formed at the dielectric ($SiO_2$)/M1 interface region. As a result, both steric effects and selective behavior of hydrazone on the surface of M1 facilitate to improve the stability of the D4 device against harsh humidity conditions.

## SN5: Hypothesis behind the surface gas-absorption process

In addition, it is vital to understand the gas absorption and reaction processes that take place on the surface of sensing materials. Since we have observed the ultra-thin M1 material with minimal roughness and record high "ON" current in negative bias region using a transistor platform, we conclude that the M1 material possesses holes as dominant charge carriers with good charge transport behavior ( Fig. S27a). When exposed to $H_2S$ gas, the M1 material showed poor sensitivity, which can be attributed to the absence of gas-specific functional groups and non-porous structures, impeding the interaction with the gas molecules. Therefore, we anticipate only a few gas molecules adsorbing on the surface, with the majority of charge carriers remaining unaffected (Fig. 27b). Previously, we know that the holes in M1 are depleted by the doped electrons from the M4 material via electrostatic attraction. These excess electrons found on the surface of M4 cause the steric effect (Fig. 27c) due to the peripheral n-alkoxy side chains. Upon $H_2S$ gas exposure, from the selectivity study, we can see that the sensitivity of D4 is roughly 64 times greater than the D1 device response. We can infer that the hydrazone M4 material is highly active in binding with $H_2S$ molecules when compared to pristine M1 material. The observed increased response of former material could be due to the presence of gas-specific secondary amine functional groups, more surface porous structures and high surface electron density. These factors might act as forerunners to absorb more $H_2S$ gas molecules, increasing the density of electrons on the surface of M4 material (Fig. 27d).

## SN6: Topography and microscopy studies of the materials with gases

The surface topography of material M4 (left) and M1 (right) is presented in the main text, Fig. 7e. The corresponding contact potential difference (CPD) map is shown in the main text, Fig. 7f. The brighter left side with high positive CPD potential indicates the presence of electrons on the surface of M4 material, aligning with our illustration in the main text, Fig. 7c. By contrast, the darker part on the right side, with a negative CPD value, indicates the probability of finding more hole matches with the concept mentioned using Fig. 7a (main text). We have exposed each sample to three gases, namely, $H_2S$, $NH_3$ and $NO_2$, and the corresponding surface potential changes are recorded. It is important to note that, after exposing the sample to the target gas, we waited for 30 minutes for complete recovery before introducing the new gas to avoid cross-contamination effects. As shown in the main text, Fig. 7g, a significant positive increase in the surface potential was observed when $H_2S$ gas molecules interacted with M4 material. Meanwhile, the surface potential of M1 material changed negligibly with the gas exposure (main text Fig. 7g). A complete recovery of the $H_2S$ exposed sample was confirmed using the surface map recorded after 30 min from exposure time (Fig. S28). Similarly, we recorded the surface potential changes of M1 and M4 materials in response to $NH_3$ and $NO_2$ gases presented in the main text, Fig. 7h and Fig. 7i, respectively. The surface potential maps indicating the recovery of the device after exposing these gases are presented in Fig. S28.

## SN7: Energy band properties of both M1 and M4 materials

We have calculated the energy bandgap ($E_{G1}$) of M1 (PDVT-10) material to be around 1.415 eV obtained using tauc plot analysis of UV-Vis spectrum (Fig. S29a). Thereafter, we used photoelectron spectroscopy in air (PESA) technique to obtain the spectrum of electron counts per second (cps) plotted against different energy levels (Fig. S29b). From the spectrum, we calculated the highest occupied molecular orbital (HOMO) of M1 to be around 5.07 eV. By subtracting EG values from HOMO results, we obtained lowest occupied molecular orbital (LUMO) valuearound 3.655 eV for M1. On the other hand, we have obtained HOMO and LUMO levels of M4 material are 5.1 and 2.9 eV, respectively, directly obtained from DFT calculation (as discussed before) as can be seen in (Fig. 7a and b in main text). From the simulation, we have also extracted the energy band gap of M4 material before ($E_{G2}$) and after ($E_{G3}$) $H_2S$ exposure is around 2.2 eV and 2.0 eV respectively.

## SN8: Optical characterizations of gas absorbent materials

The emission spectra recorded for the M4 dissolved in dimethylformamide (DMF) and dichloromethane (DCM) and drop-cast thin film during the presence and absence of $H_2S$ gas (Fig. S30). Likewise, the UV-Vis spectra of M4 in DMF, DCM and thin film are presented in Fig. S31. The apparent changes in the spectral pattern, namely, an decrease/increase in the peak intensities or splitting of peaks or the fading of bands, indicate that the material M4 after exposure to $H_2S$ gas changes its photophysical property. Investigating the photophysical behavior of fluorescent discotic is vital, especially given the thought that they can be incorporated into devices as charge-carrier transport layers.[4] Thus, the long-armed tris(keto-hydrozone) discotics (M2, M3 and M4) realized in this work were subjected to their UV–Vis-NIR absorption and photoluminescence spectral studies. All the tris(keto-hydrozone) compounds synthesized are wine-red solids. The M4 material alone was used in the $H_2S$ sensing experiment. The absorption spectra of the M4 was carried out using DCM and DMF, and was found to be virtually identical (Fig. S31), comprising three intense absorption peaks center around. 275, 370 and 490 nm, which can be assigned to $\pi$-$\pi^*$ and n-$\pi^*$ transitions. The M4 in DCM and DMF bubbled with a small amount of $H_2S$ gas, as shown in Fig. S31. The apparent changes in the spectral pattern was observed, namely, a decrease in the peak intensity (Fig. S31c) and fading of bands with an increase in intensity, with the intense peak around 437 nm (Fig. S31a) indicating that M4 changes its photophysical behavior. When excited with light of around 380 nm wavelength, these solutions show an emission band centered around 570 nm (Fig. S30a,b). The decrease in peak intensities of emission spectra confirms the interactions of $H_2S$ with M4.

The absorption and emission spectra of the M4 thin film sample, prepared by the drop-casting method, was recorded at room temperature. Absorption spectra of thin film before and after expose to $H_2S$ gas were found to be identical, with peaks of around 270, 375 and 490 nm (Fig. S31c). The corresponding data showed practically indistinguishable spectra, with a prominently broad emissive band around 630 nm (Fig. S30c) for pristine sample. The noticeable changes in the emission spectral pattern after exposure to $H_2S$ gas, that is, a drastic decrease in intensity, undoubtedly indicate that the M4 changes its photophysical behavior. This can be accredited to the strong association of M4 and $H_2S$ molecules. The ionization potential (IP) of both M1 and M4 materials were explored using photoelectron spectroscopy in air (PESA). This instrument is equipped with special detectors that have the capability to count the electrons ejected from the sample when it is excited by the electromagnetic waves whose energies span from 3.0 eV to 6.5 eV. To avoid manual calculation errors, AC-2 software, specially designed to record the PESA data, allows us to perform required data fitting with high-level accuracy and automatically generates the IP values of the tested materials.

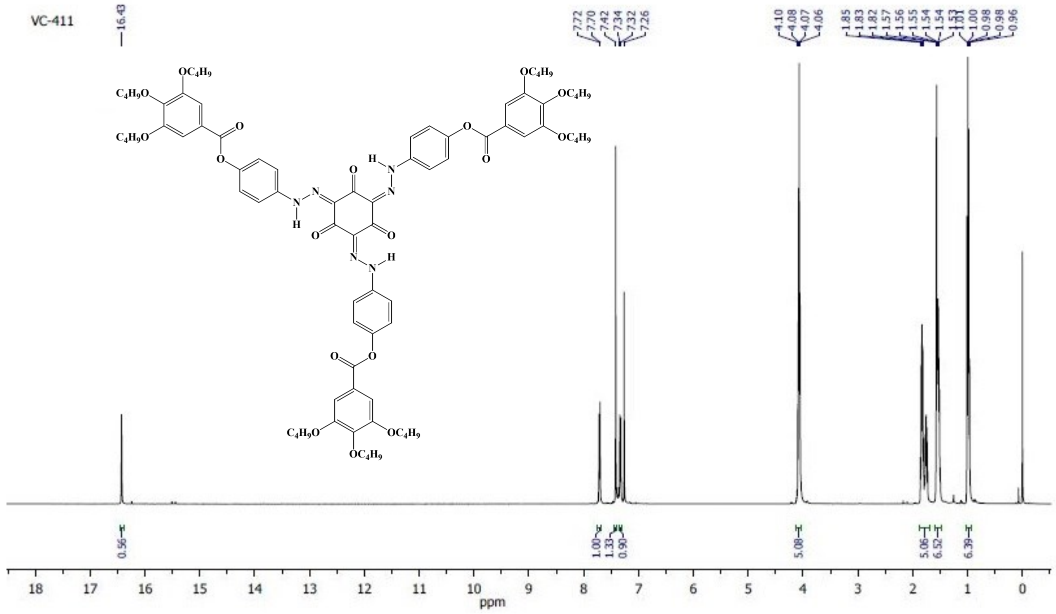

**Fig S1A.** 1H NMR spectrum of compound HDN4 (400MHz; CDCl3)

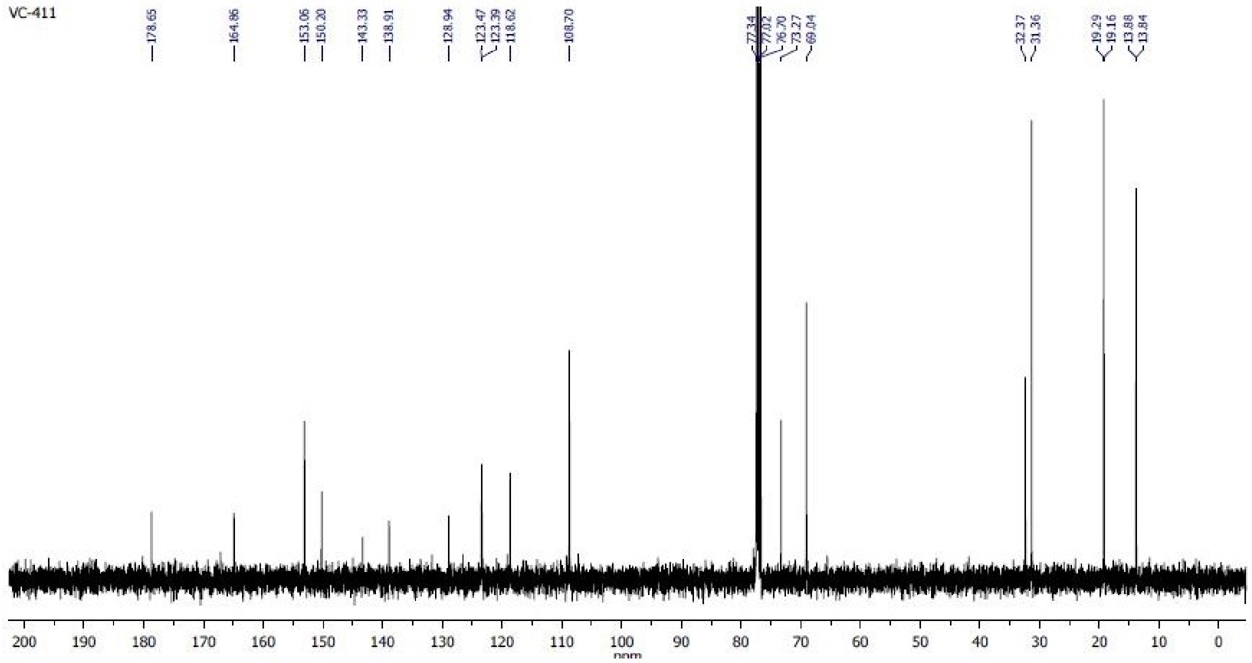

**Fig S1B**. $^{13}C$ NMR spectrum of compound **HDN4** (100MHz; CDCl3)

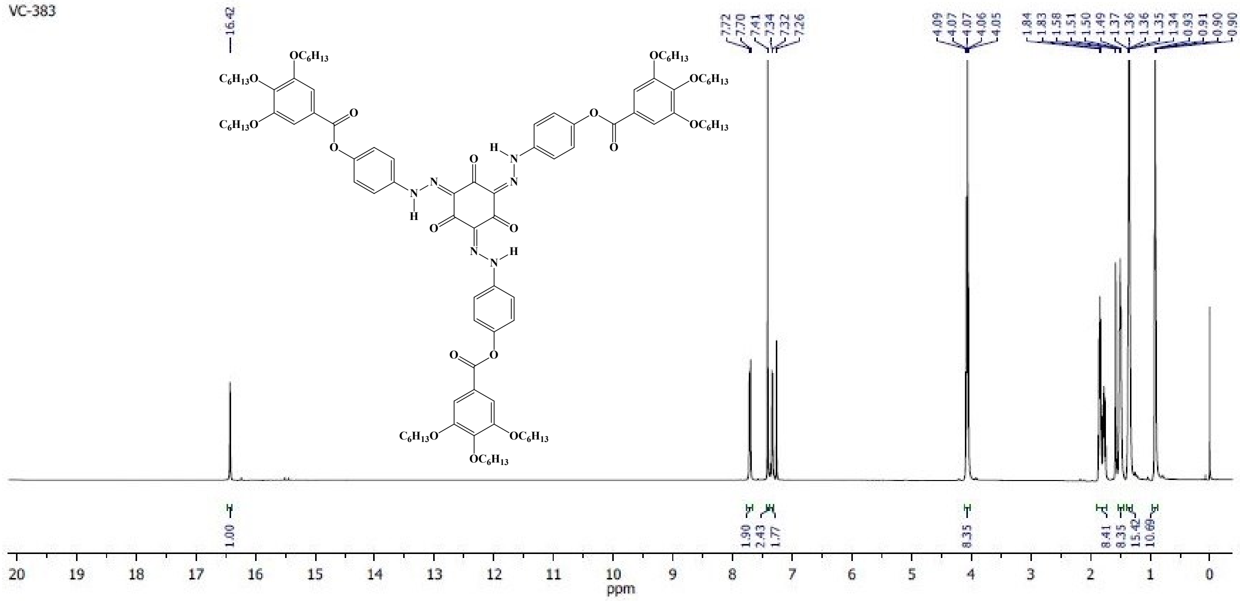

**Fig S2A**. $^{1}H$ NMR spectrum of compound **HDN6** (400MHz; CDCl3)

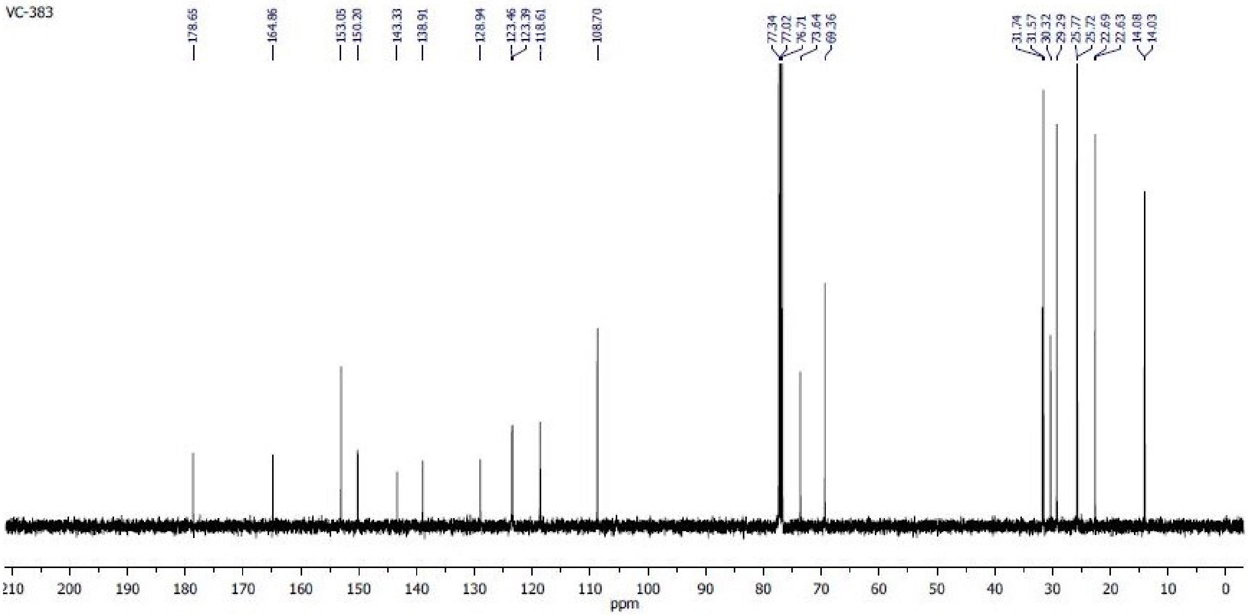

**Fig S2B**. $^{13}$C NMR spectrum of compound **HDN6** (100MHz; CDCl3)

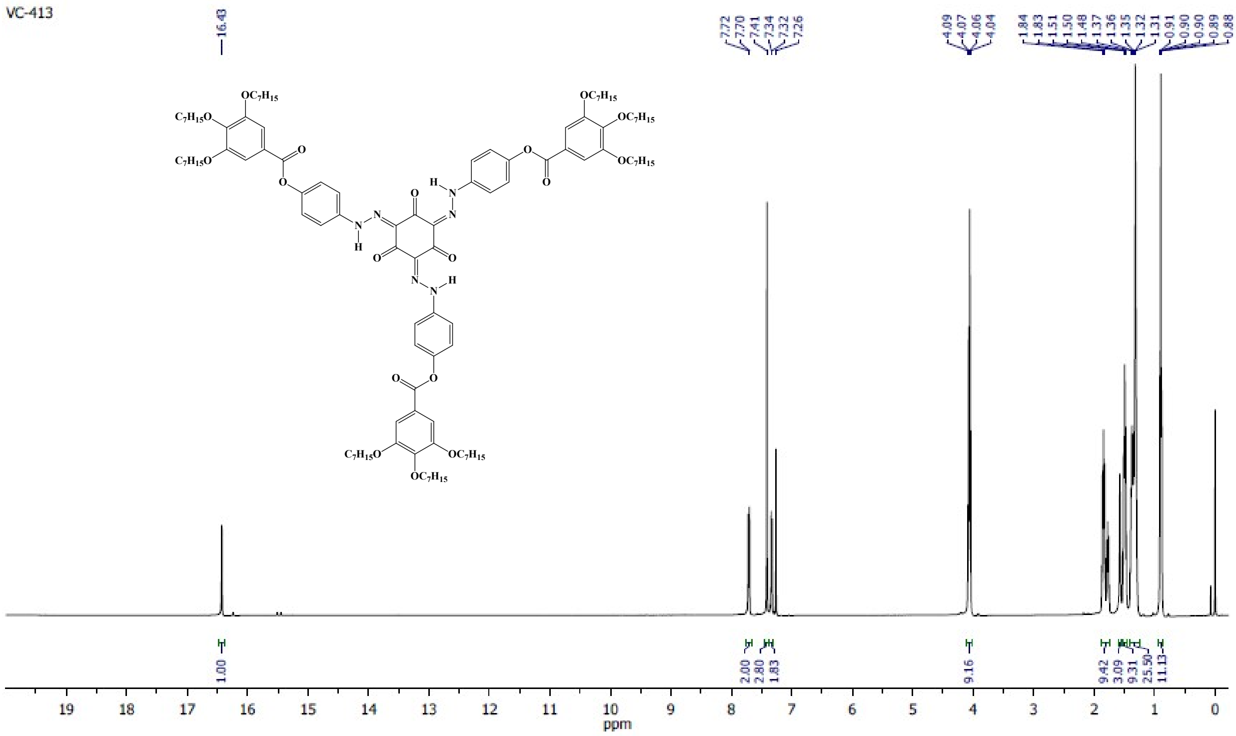

**Fig S3A**. $^{1}$H NMR spectrum of compound **HDN7** (400MHz; CDCl3)

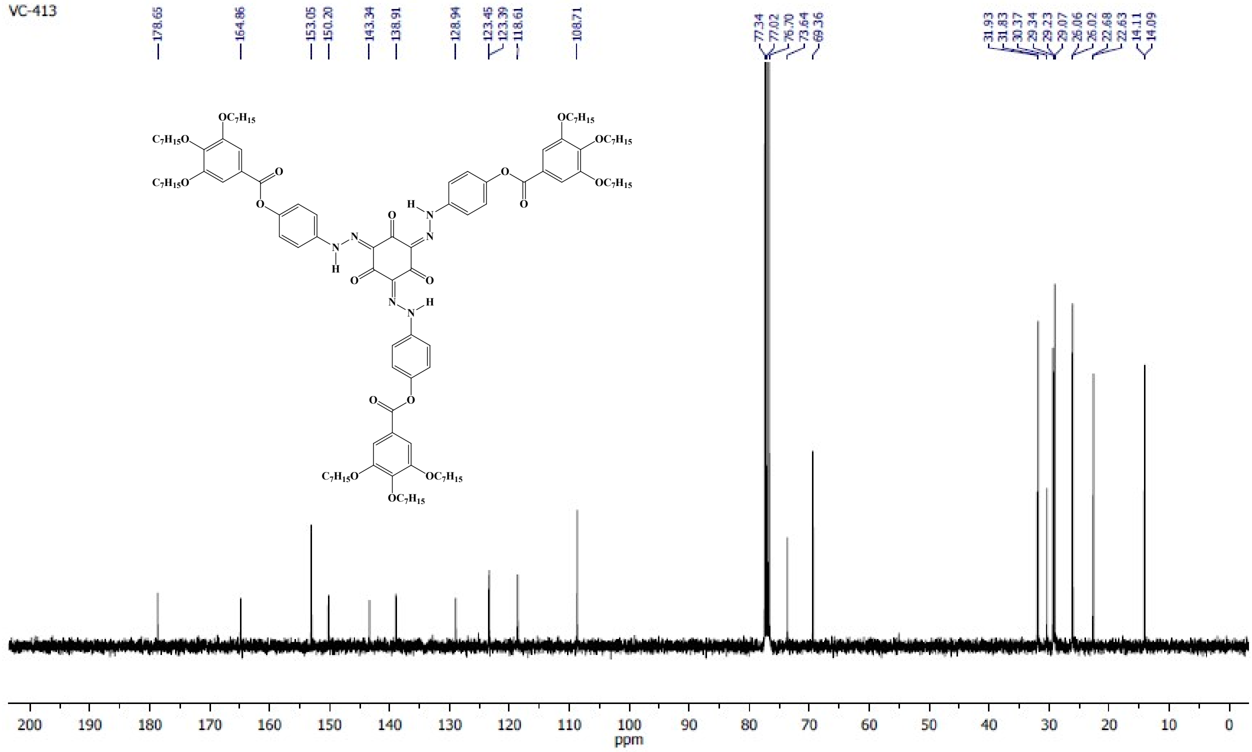

**Fig S3B**. $^{13}$C NMR spectrum of compound **HDN7** (100MHz; CDCl3)

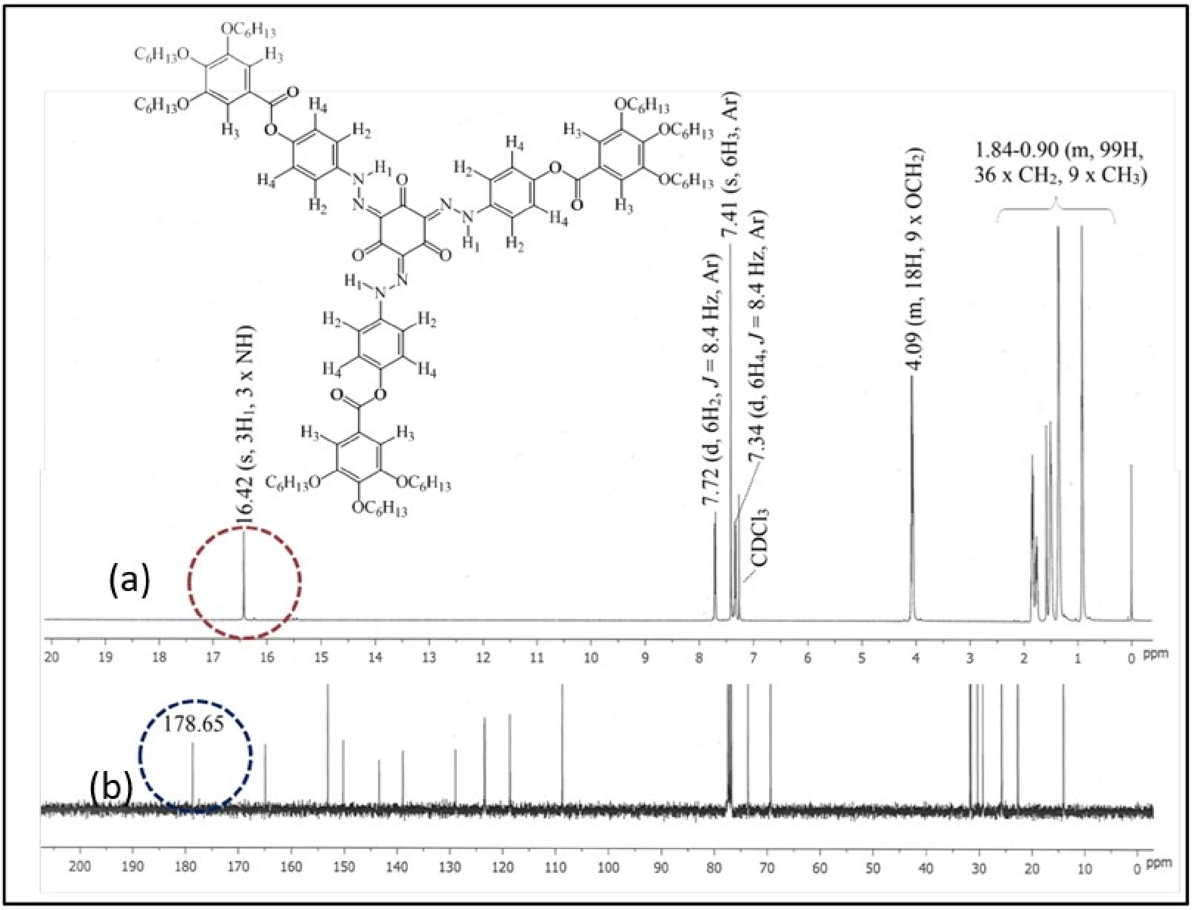

**Fig. S4**. $^{1}$H (a) & $^{13}$ NMR (b) spectra of **M3 (HDN6)** in CDCl$_3$ recorded at room temperature

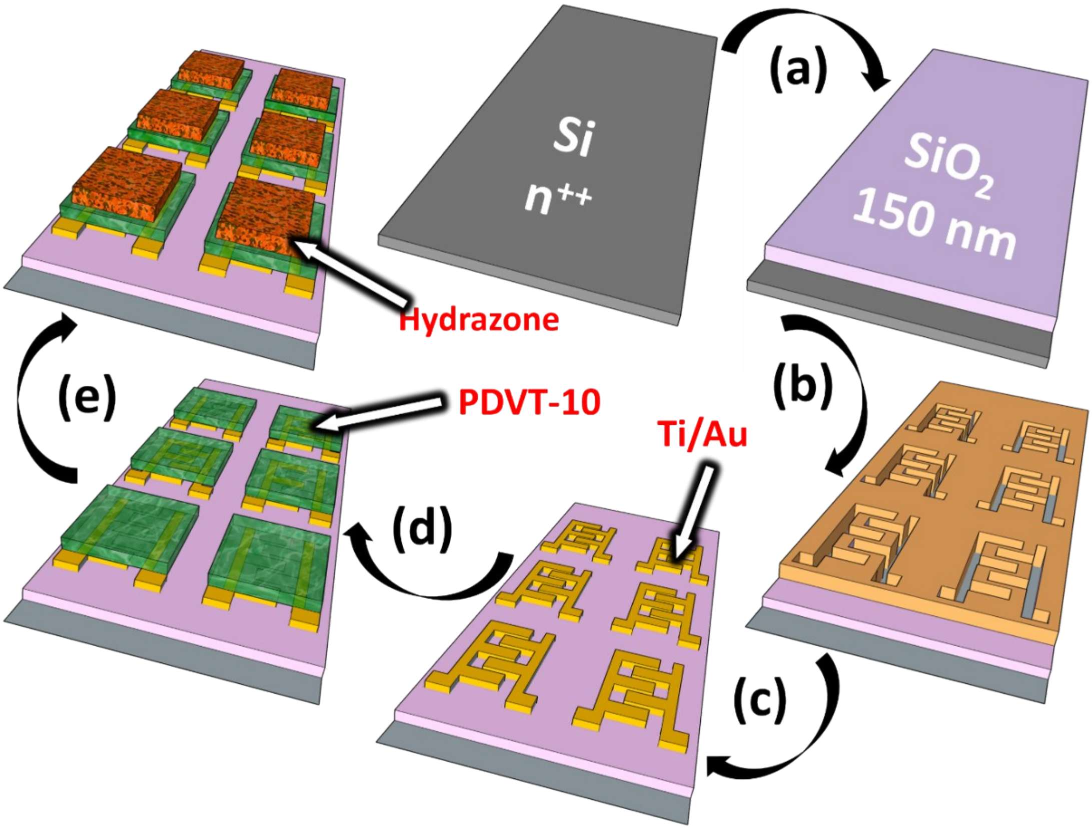

**Fig. S5 OFET device fabrication process**. (a) Dielectric oxide growth step - We have employed a thermal growth system and the process parameters were optimized to grow 150 nm $SiO_2$ dielectric, using a dry oxide approach, on the surface of highly doped Si. (b) Photolithography and development process- Then, AZ5214 photoresist was spin-coated on the surface of $Si/SiO_2$ substrate. The photoresist-coated substrate was subjected to photolithography process to image the interdigitated electrodes design on the surface of resist. The exposed sample is developed to imprint the electrode design on the surface of the substrate. (c) Electrode deposition and lift-off step – After the development process, the sample was taken to a physical deposition system to deposit the Ti (10 nm) and Au (100 nm) sequentially to obtain Ti/Au stack. Then we have executed lift-off technique in acetone using ultrasonicator bath to remove the photoresist, along with metals, from the substrate to form source and drain Ti/Au interdigitated electrodes (IDE) on top of $Si/SiO_2$ substrate. d PDVT-10 film formation process – Using the optimized recipe, the as-prepared PDVT-10 organic semiconductor solution was spin-coated and patterned in the IDE electrode region. After deposition, the PDVT-10 coated sample was suspended on the hotplate for 10 min @ 180 °C. (e) The tris(keto-hydrazone) was dissolved in chloroform to prepare a 5mg/0.5mL solution. 4 µL of this solution was drop cast on the surface of the PDVT-10 coated $Si/SiO_2$ substrate. Hence, we have fabricated the hydrazone/PDVT-10 OFET devices.

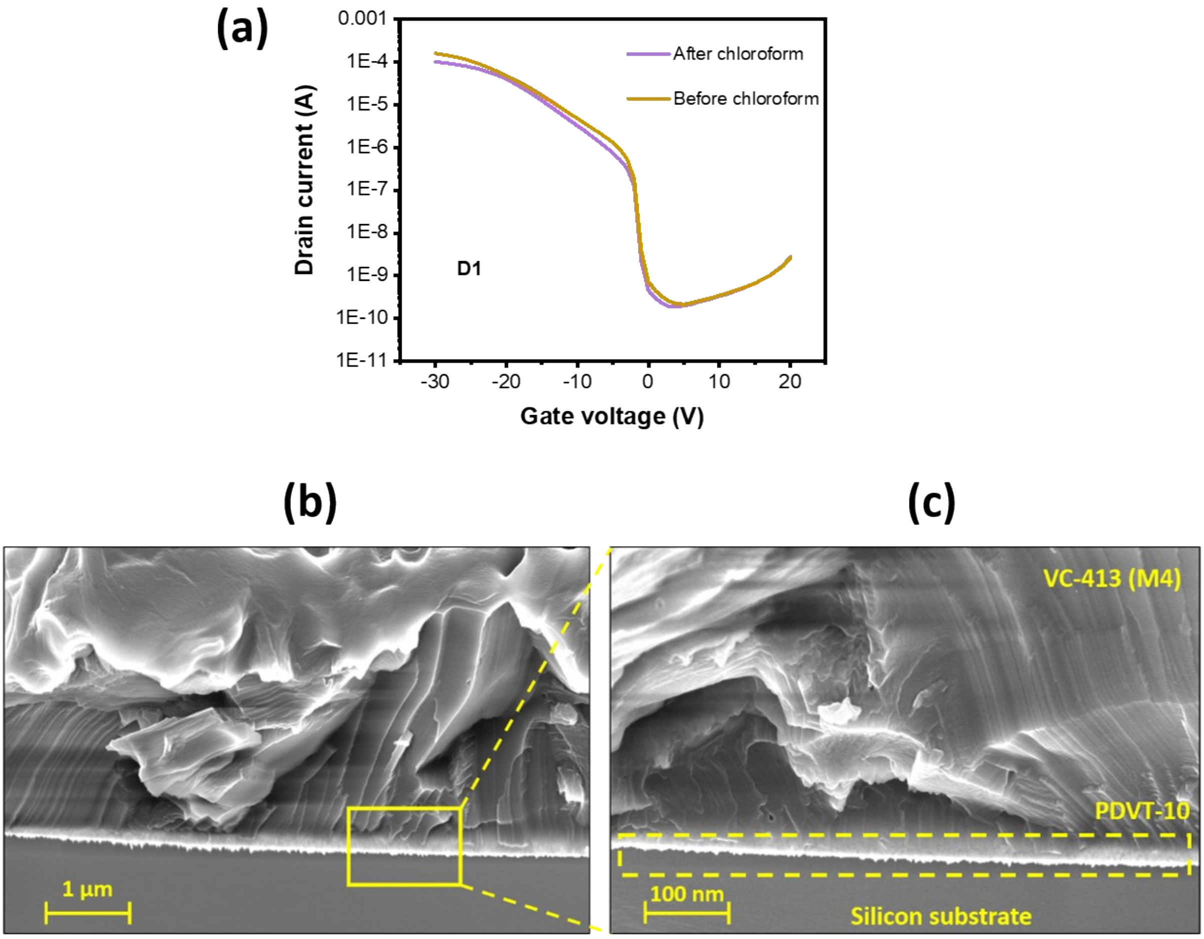

**Fig. S6 Device stack characterization:**: (a) Studying the effect of chloroform on PDVT-10 OFET device. (b) Low and (c) High resolution cross section FESEM images of PDVT-10/tris(keto-hydrazone) on the substrate.

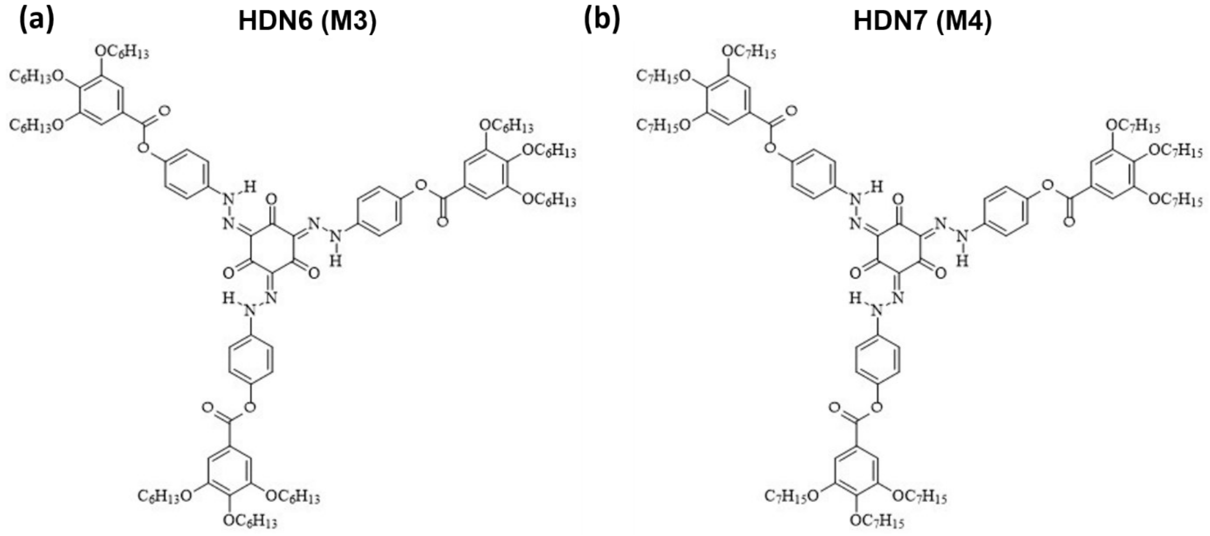

**Fig. S7 Molecular structures of gas absorbent layers**: (a) HDN6 (M3) and (b) HDN7 (M4) materials.

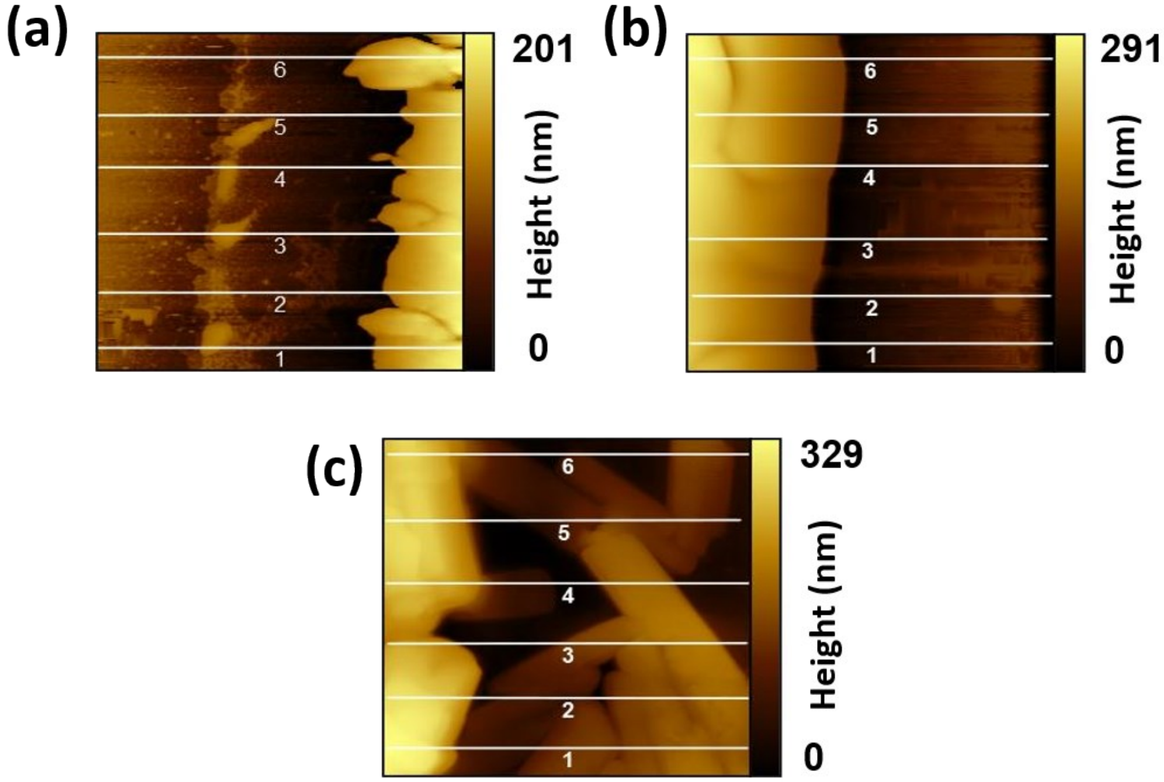

**Fig. S8 Surface Atomic force microscopy (AFM) characterization of tris(keto-hydrazone) materials.** AFM topography maps of (a) M2, (b) M3 and (c) M4 materials (thickness averaged from 6 different points).

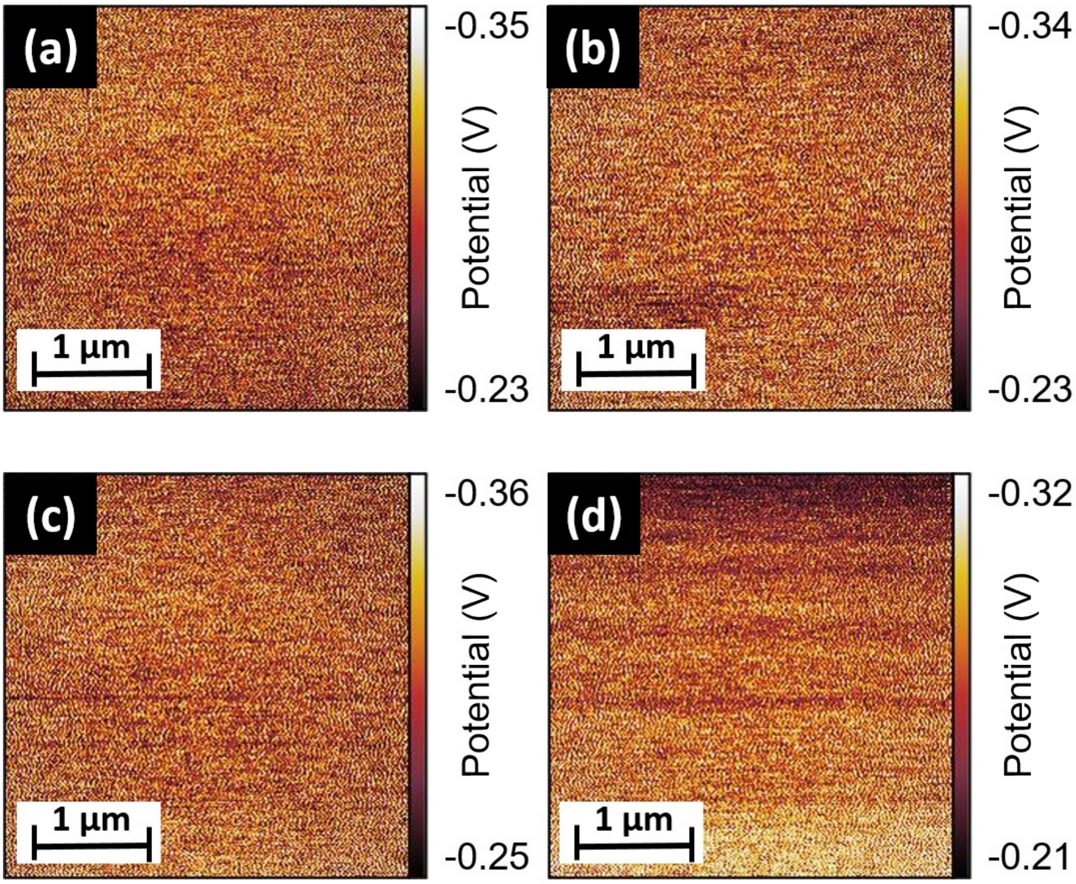

**Fig. S9 Surface Kelvin probe force microscopy (KPFM) characterization of standard HOPG sample.** KPFM maps of HOPG calibration sample taken before testing (a) M1, (b) M2, (c) M3 and (d) M4 materials.

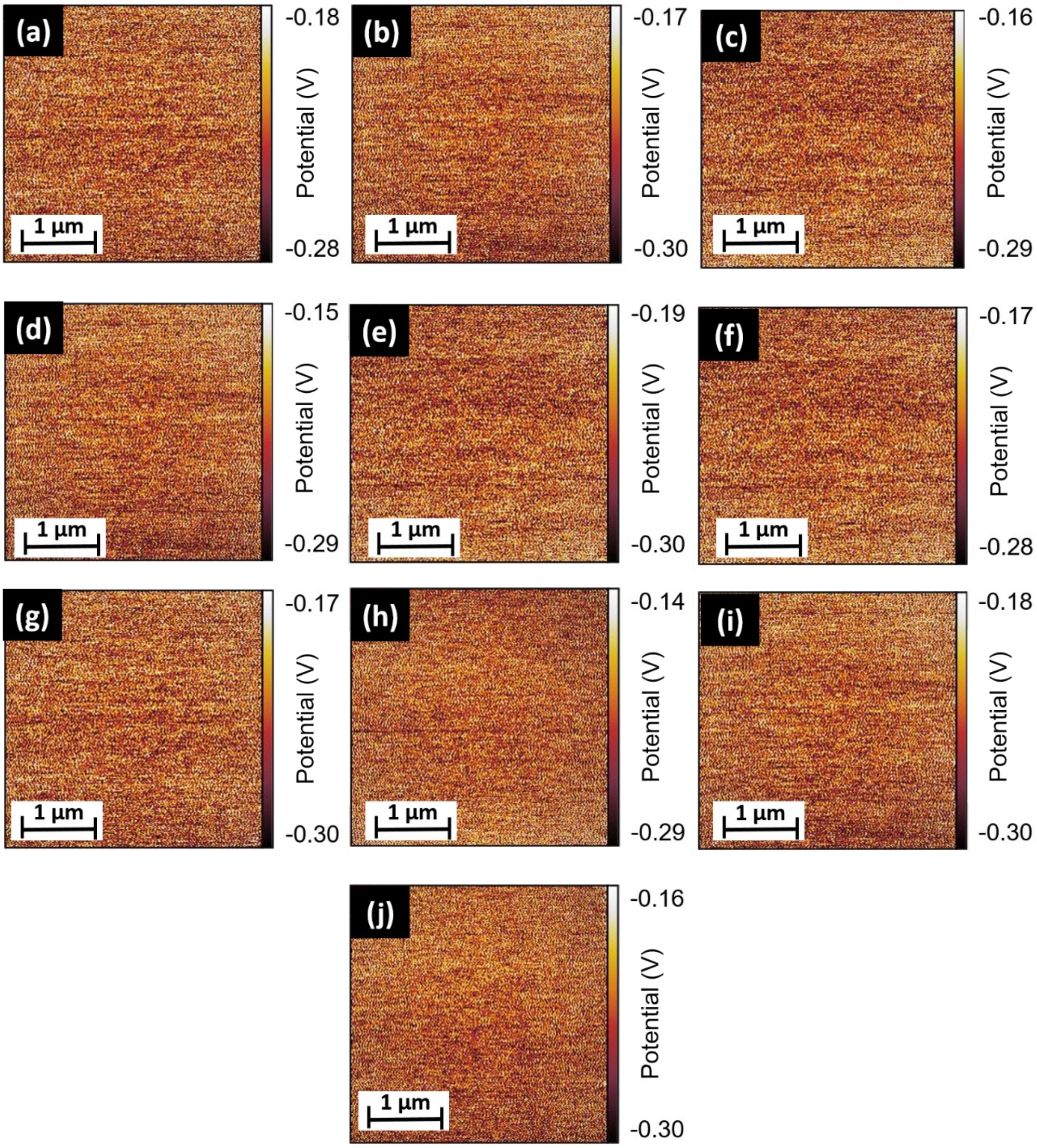

**Fig. S10 KPFM characterization of M1.** (a-j) CPD maps obtained after scanning 10 different locations on the surface of M1 material.

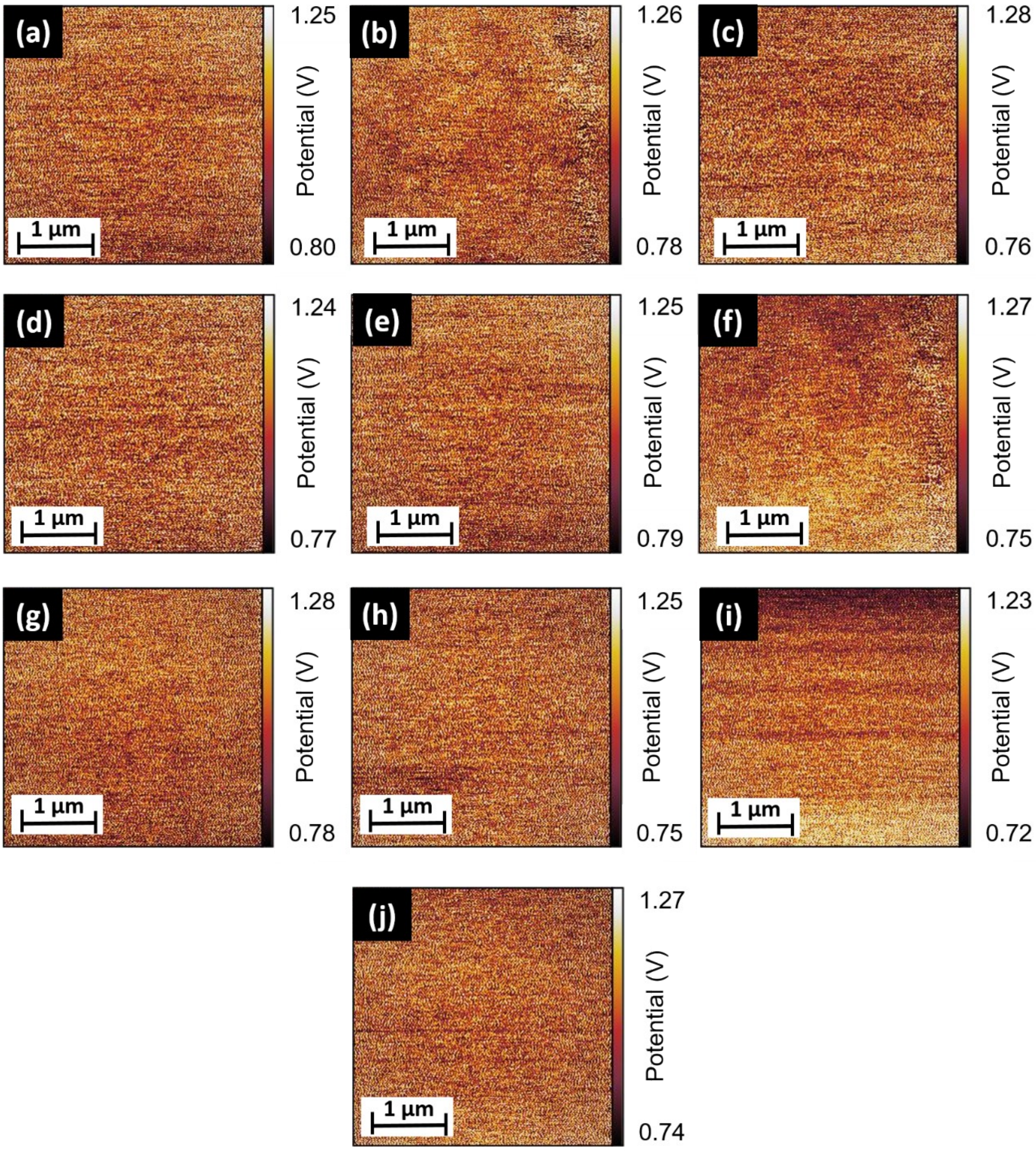

**Fig. S11 KPFM characterization of M2.** (a-j) CPD maps obtained after scanning 10 different locations on the surface of M2 material.

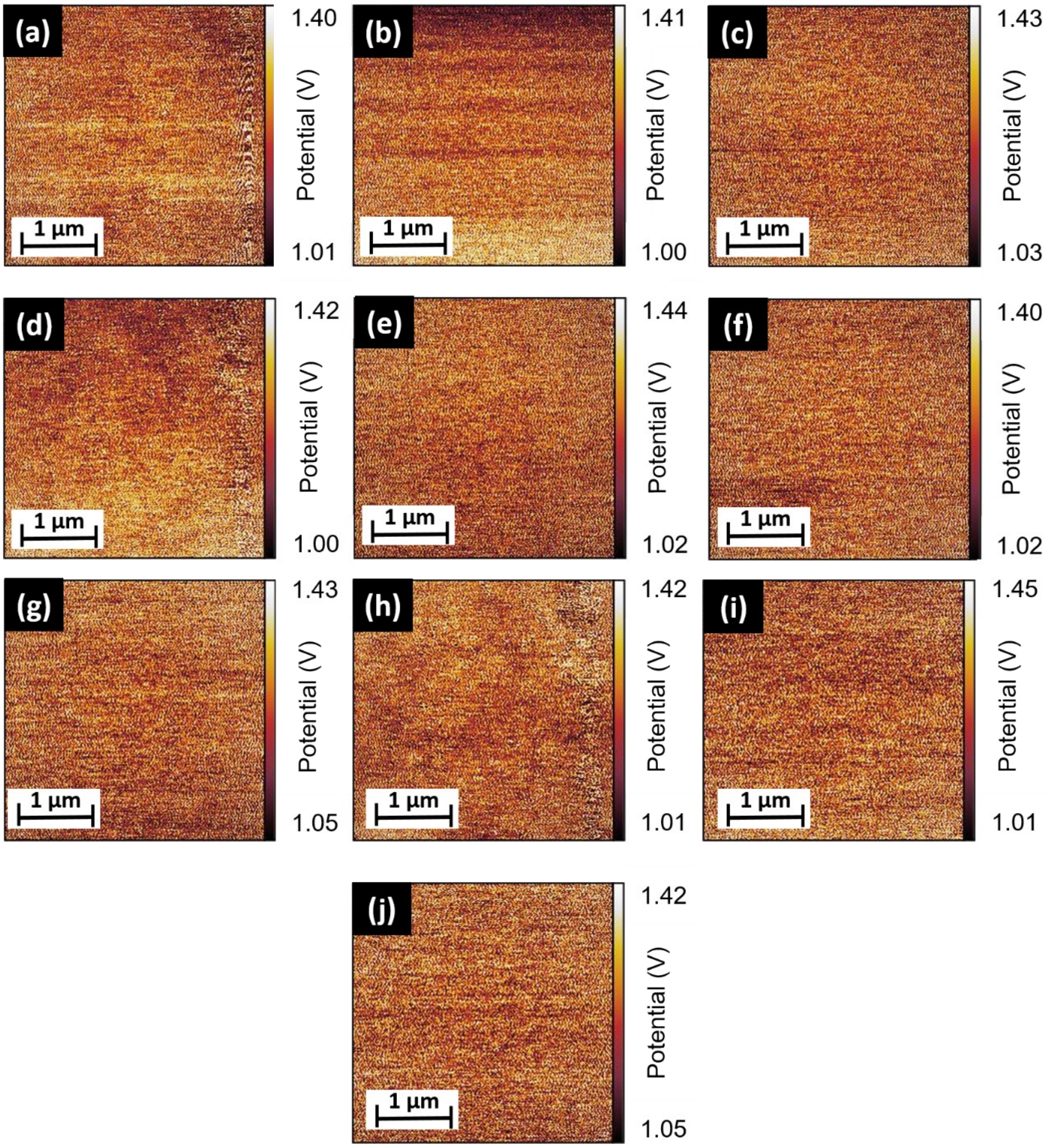

**Fig. S12 KPFM characterization of M3.** (a-j) CPD maps obtained after scanning 10 different locations on the surface of M3 material.

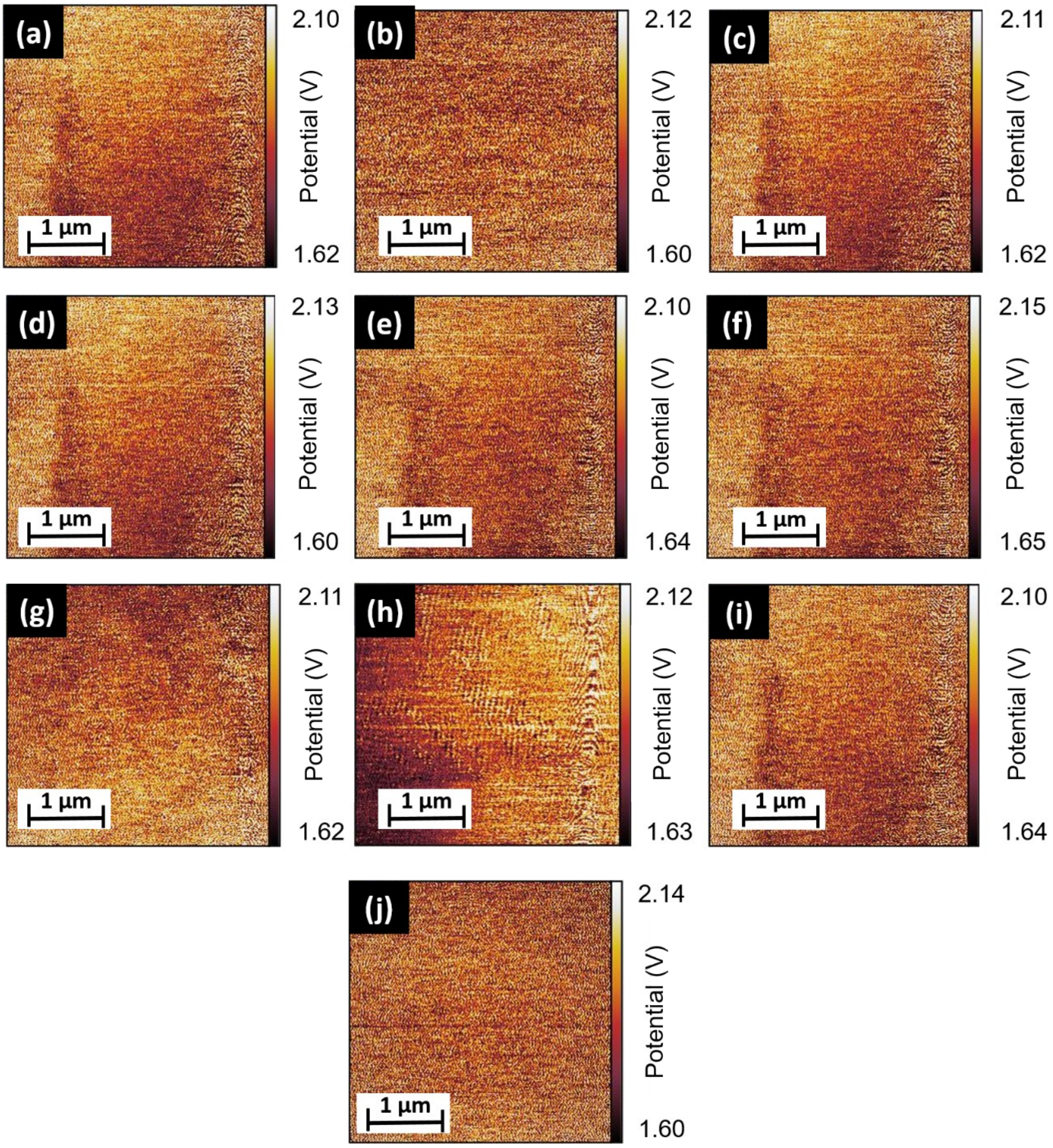

**Fig. S13 KPFM characterization of M4.** (a-j) CPD maps obtained after scanning 10 different locations on the surface of M4 material.

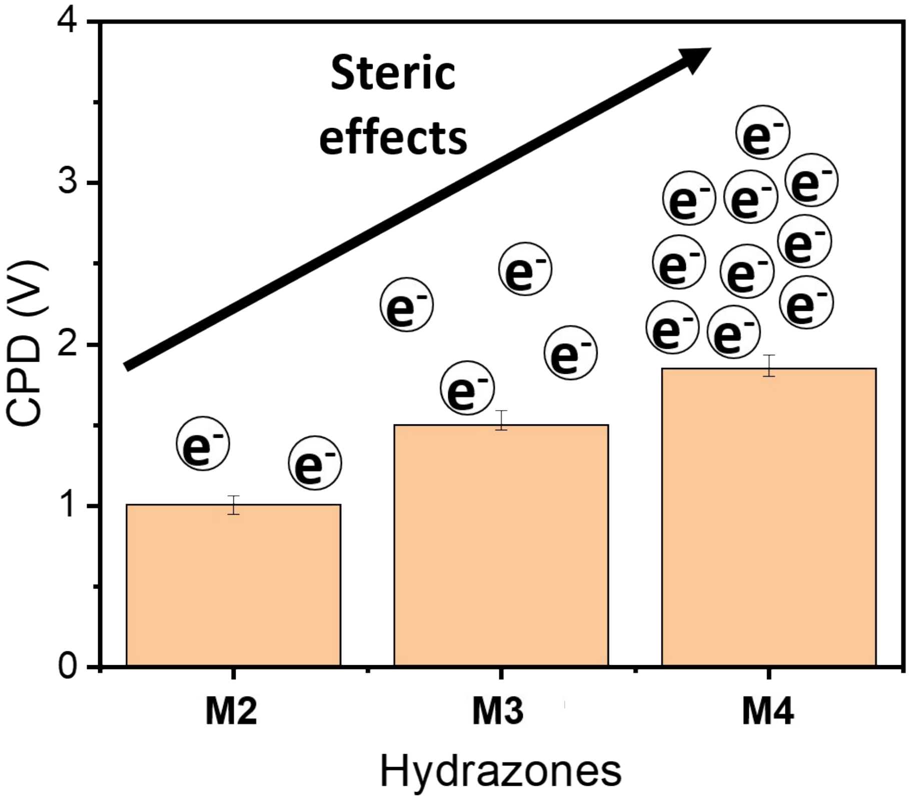

**Fig. S14 Surface potential values for different tris(keto-hydrazone) materials**. Contact potential difference (CPD) values for M2, M3 and M4 materials are plotted. The inset signifies the peripheral chain length-dependent steric effect increases with the CPD values from M2 to M4.

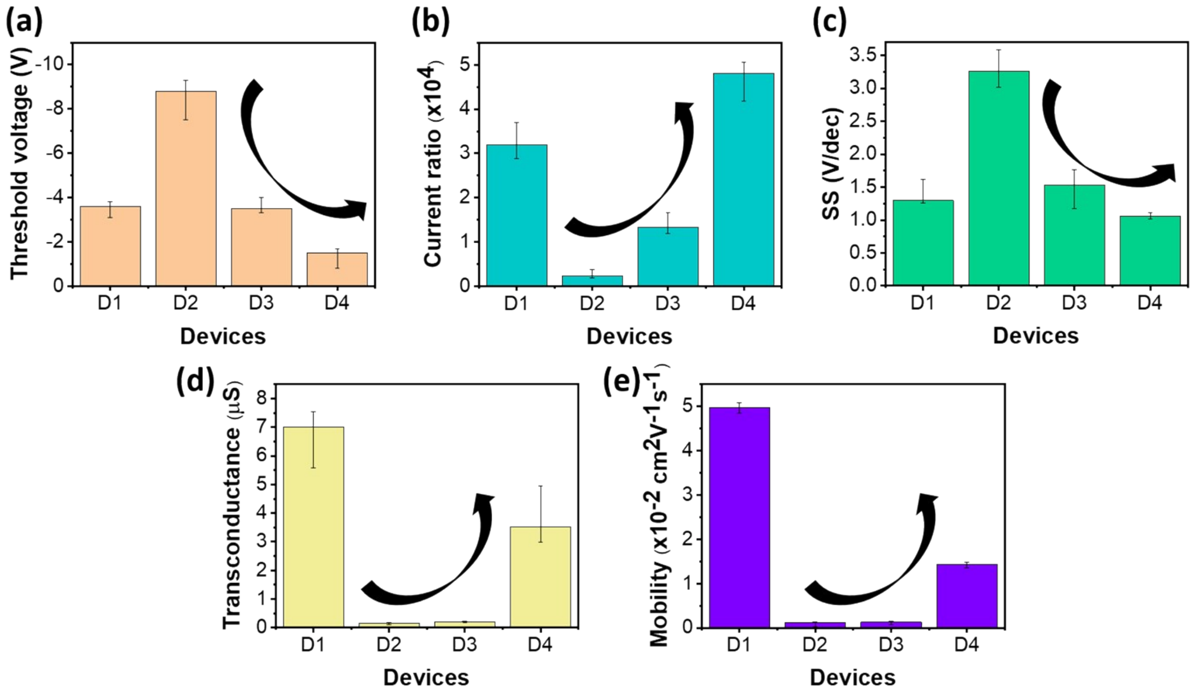

**Fig. S15 Electrical characterization of the OFET devices.** Transistor parameters such as (a) Threshold voltage, (b) Current ratio, (c) Subthreshold swing (SS), (d) Transconductance, (e) Mobility values are plotted against different devices. The inset arrows indicate the trend followed by transistor parameters for different OFET devices (D2-D4).

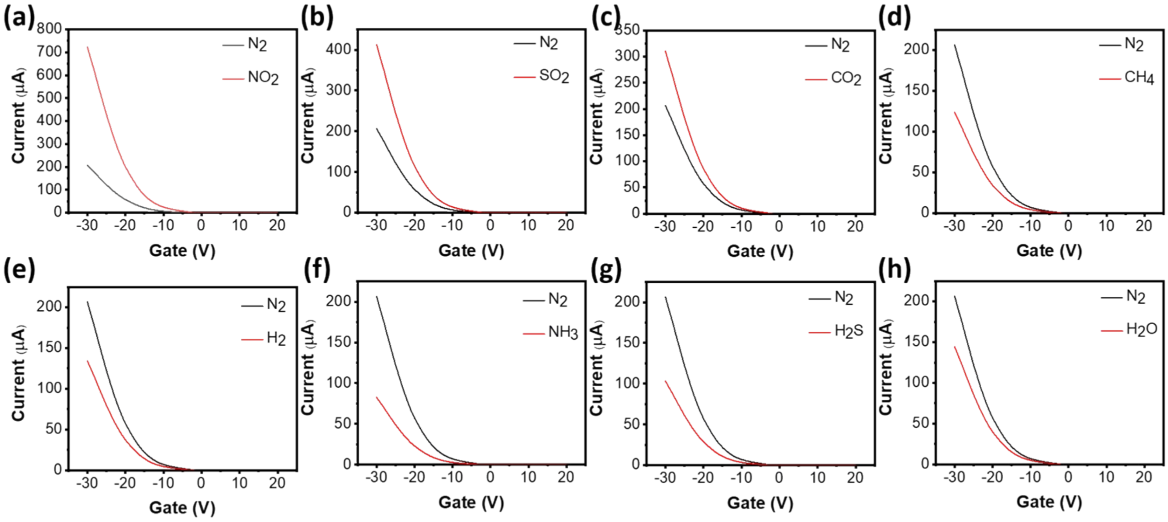

**Fig. S16 Pristine D1OFET device characteristics in the presence of gases**. Transfer characteristic of D1 OFET device toward (a) $NO_2$ (50 ppm), (b) $SO_2$ (50 ppm), (c) $CO_2$ (50 ppm), (d) $CH_4$ (50 ppm), (e) $H_2$ (50 ppm), (f) $NH_3$ (50 ppm), (g) $H_2S$ (50 ppm) and (h) $H_2O$ (90% RH) analytes.

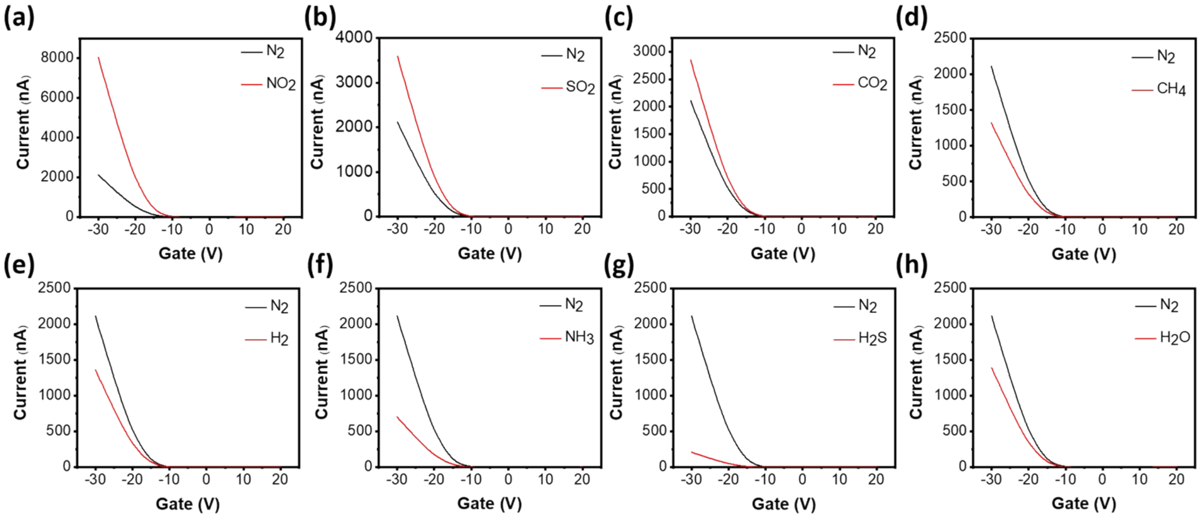

**Fig. S17 D2 OFET device characteristics in the presence of gases.** Transfer characteristic of D2 OFET device toward (a) $NO_2$ (50 ppm), (b) $SO_2$ (50 ppm), (c) $CO_2$ (50 ppm), (d) $CH_4$ (50 ppm), (e) $H_2$ (50 ppm), (f) $NH_3$ (50 ppm), (g) $H_2S$ (50 ppm) and (h) $H_2O$ (90% RH) analytes.

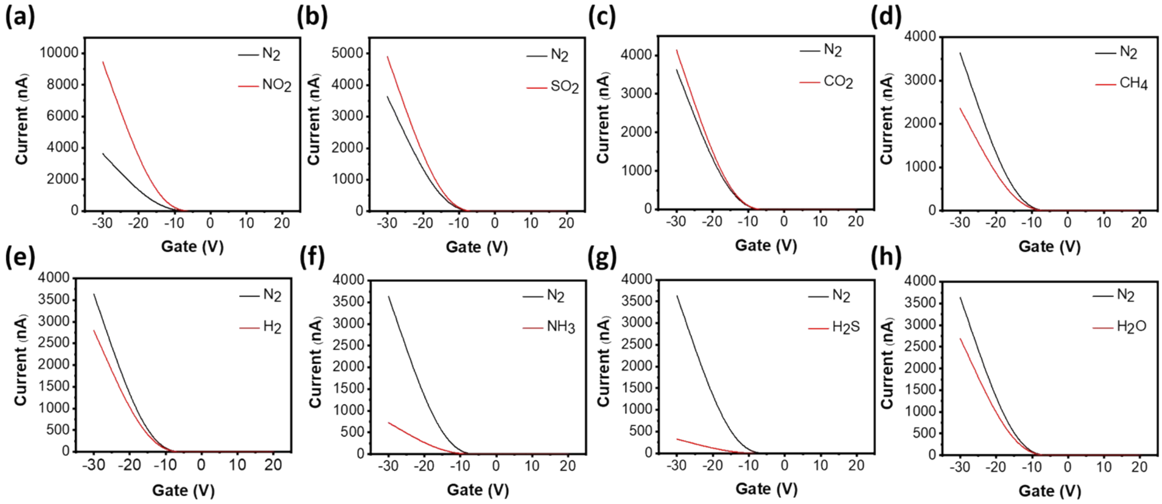

**Fig. S18 D3 OFET device characteristics in the presence of gases**. Transfer characteristic of D2 OFET device toward (a) $NO_2$ (50 ppm), (b) $SO_2$ (50 ppm), (c) $CO_2$ (50 ppm), (d) $CH_4$ (50 ppm), (e) $H_2$ (50 ppm), (f) $NH_3$ (50 ppm), (g) $H_2S$ (50 ppm) and (h) $H_2O$ (90% RH) analytes.

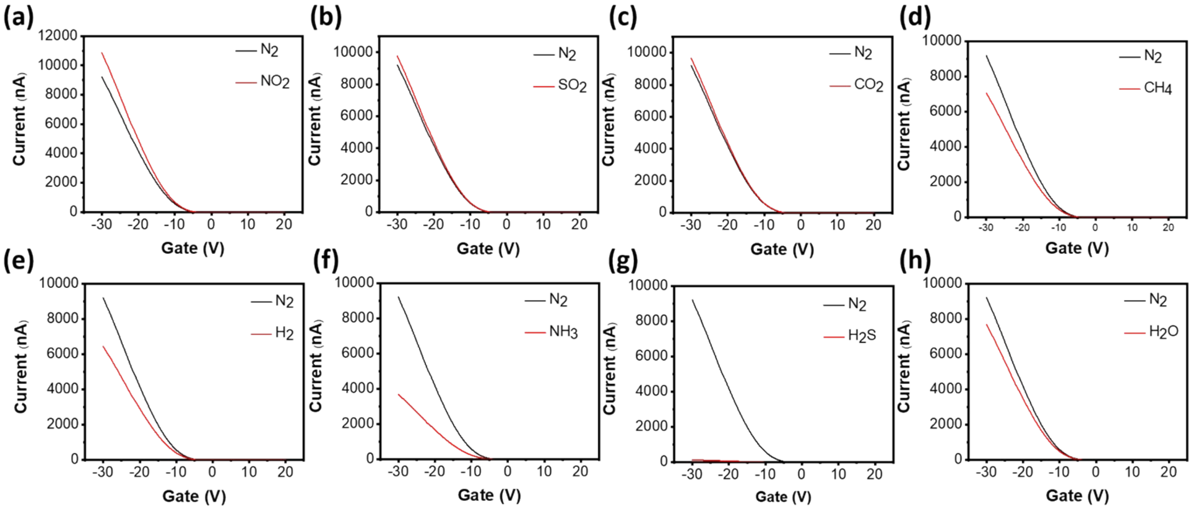

**Fig. S19 D4 OFET device characteristics in the presence of gases**. Transfer characteristic of D2 OFET device toward (a) $NO_2$ (50 ppm), (b) $SO_2$ (50 ppm), (c) $CO_2$ (50 ppm), (d) $CH_4$ (50 ppm), (e) $H_2$ (50 ppm), (f) $NH_3$ (50 ppm), (g) $H_2S$ (50 ppm) and (h) $H_2O$ (90% RH) analytes.

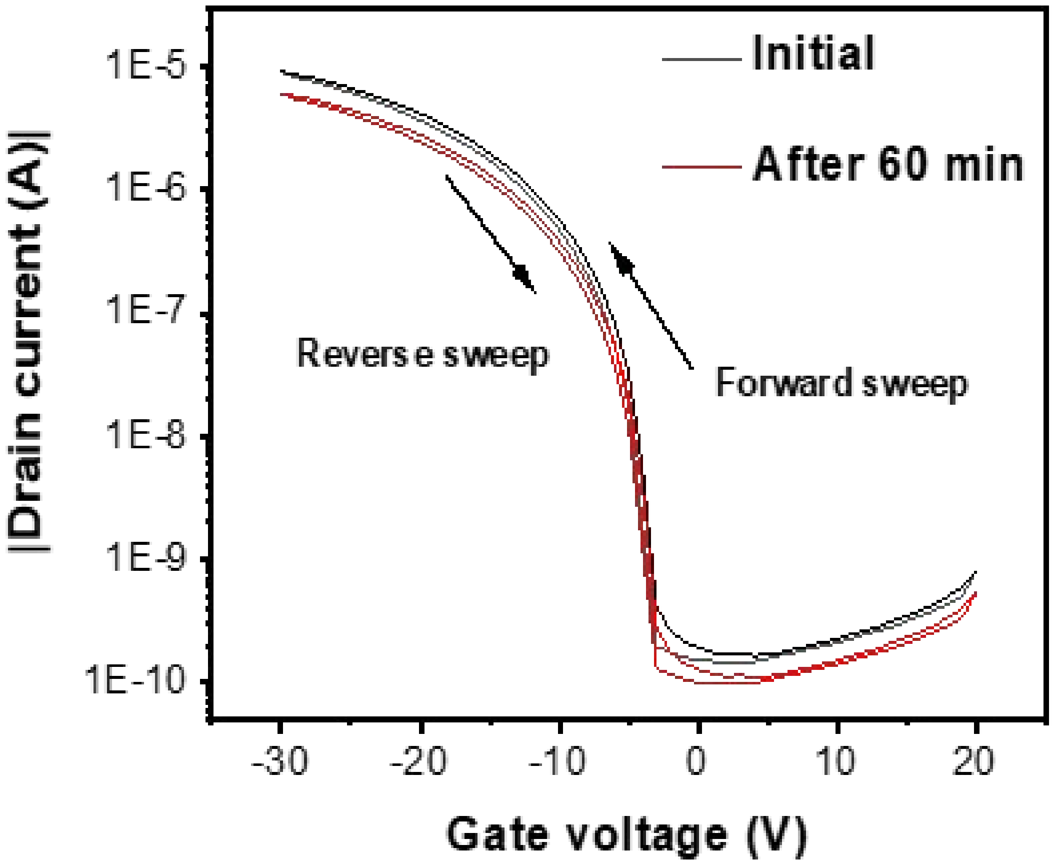

**Fig. S20** Hysteresis effect study on D4 device for a period of an hour.

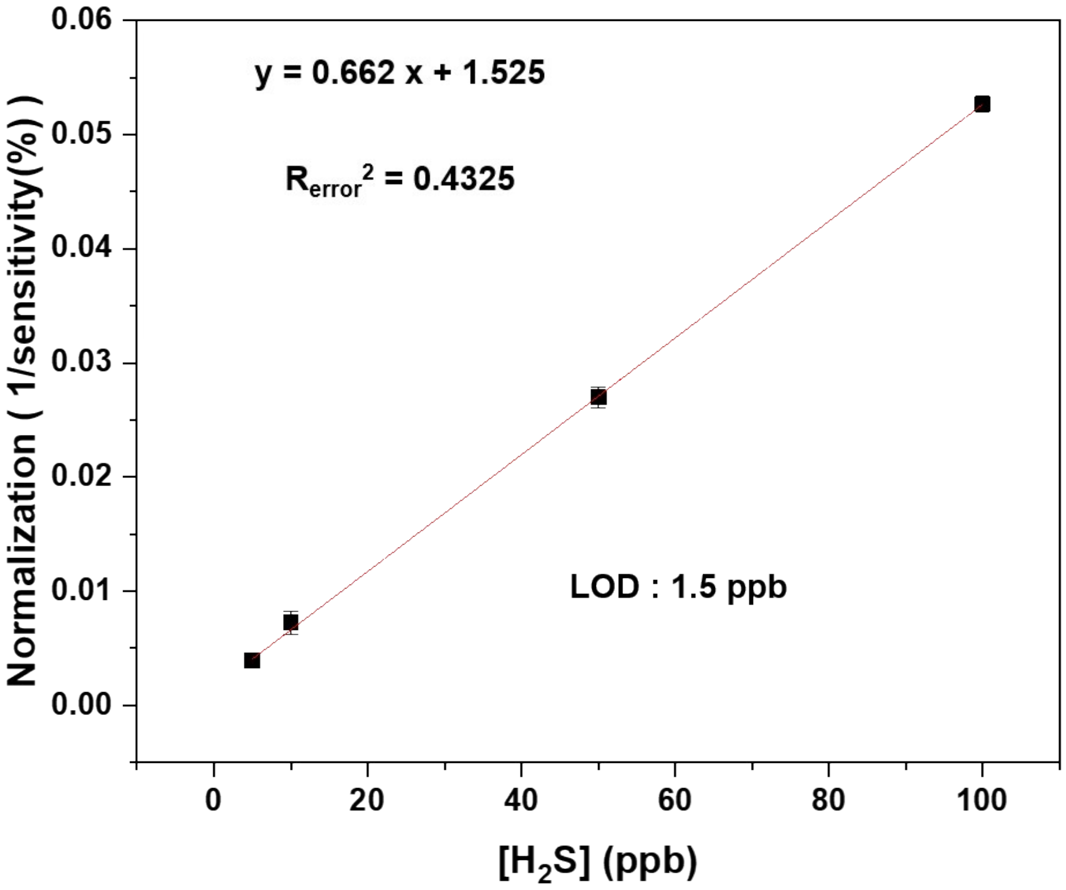

**Fig. S21 Calculation of Limit of Detection (LOD) detection**. Theoretical LOD of D4 OFET $H_2S$ sensor is calculated using the Root mean square method (RMS).

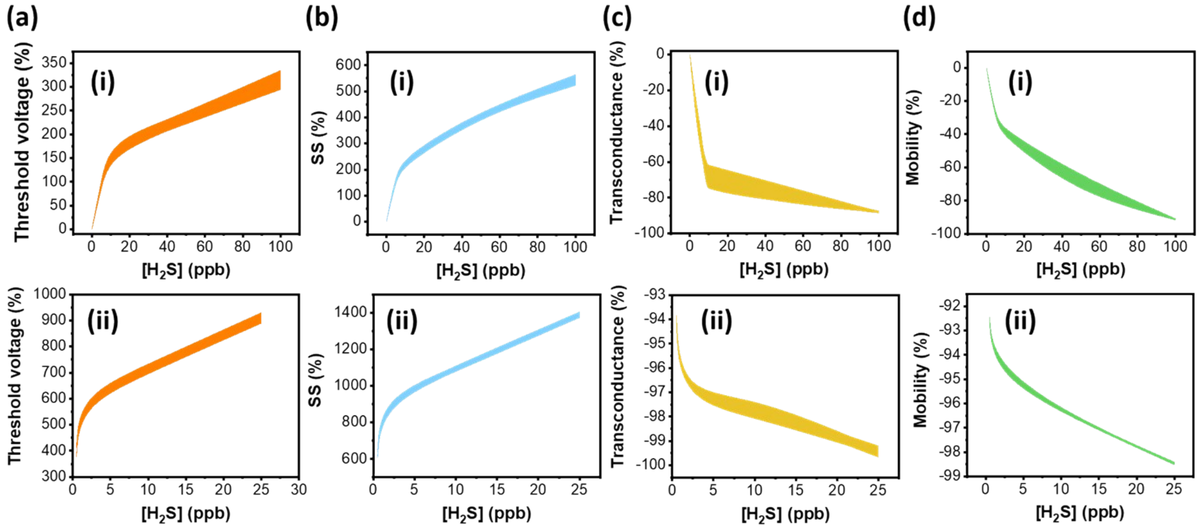

**Fig. S22 Electrical characterization of D4 OFET device in the presence of H2S gas**. Transistor parameters such as (a) Threshold voltage, (b) Subthreshold swing (SS), (c) Transconductance and (d) Mobility are plotted against the $H_2S$ gas concentrations lies in (i) 0-100 ppb and (ii) 0.1-25 ppm.

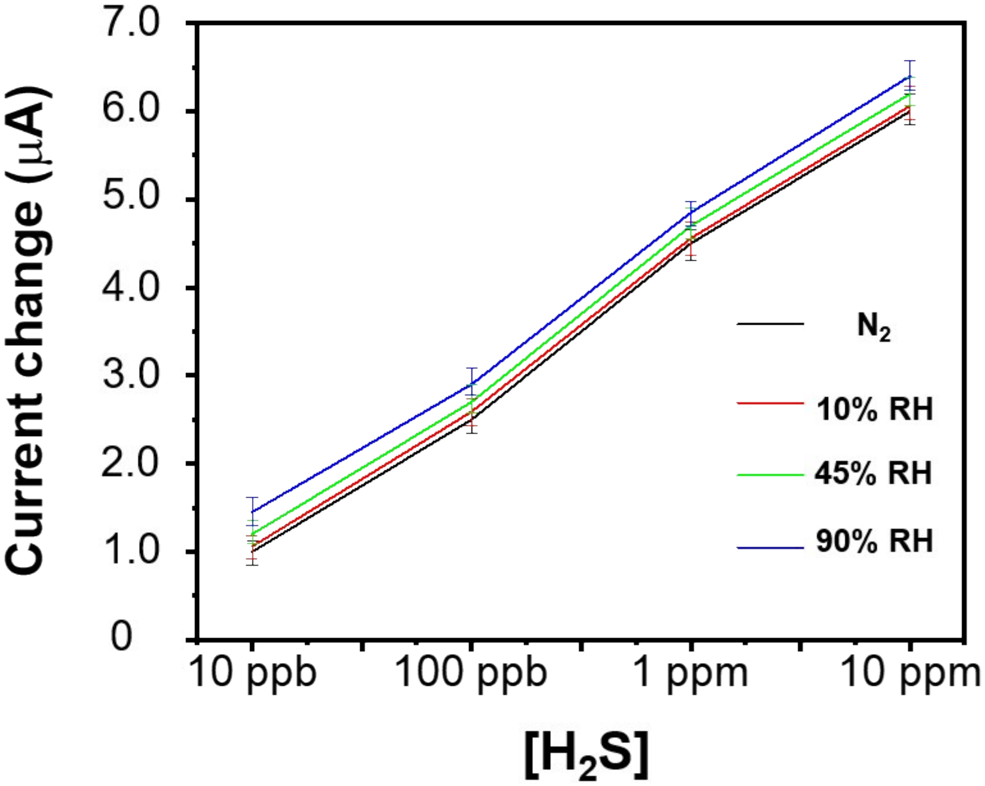

**Fig. S23 Effect of humidity on gas response**. Current response is recorded from D4 OFET devices and plotted against different $H_2S$ gas concentrations (10 ppb, 100 ppb, 1 ppm and 10 ppm) in presence of $N_2$, 10% RH, 45% RH and 90% RH conditions controlled in the gas testing chamber.

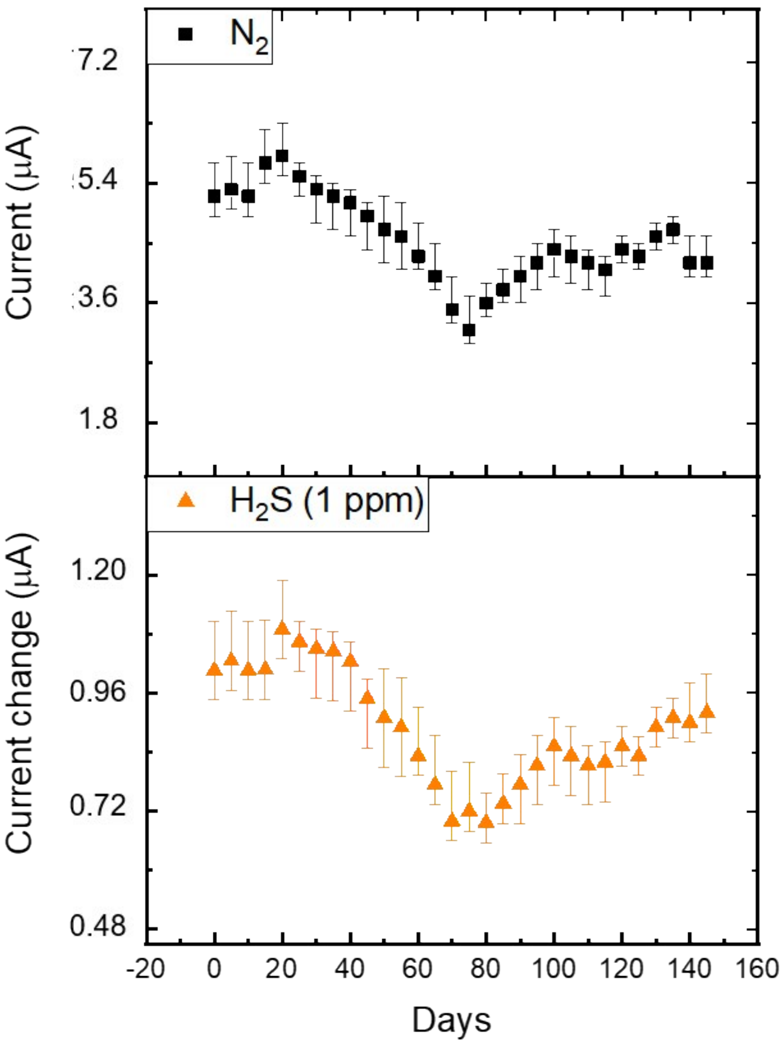

**Fig. S24 Ambient stability of D2 OFET sensor**. Stability of the D2 OFET device was monitored for a total of 150 days by recording the current response under (top) $N_2$ inert atmosphere and (bottom) $H_2S$ (1 ppm) gas for every 5 days.

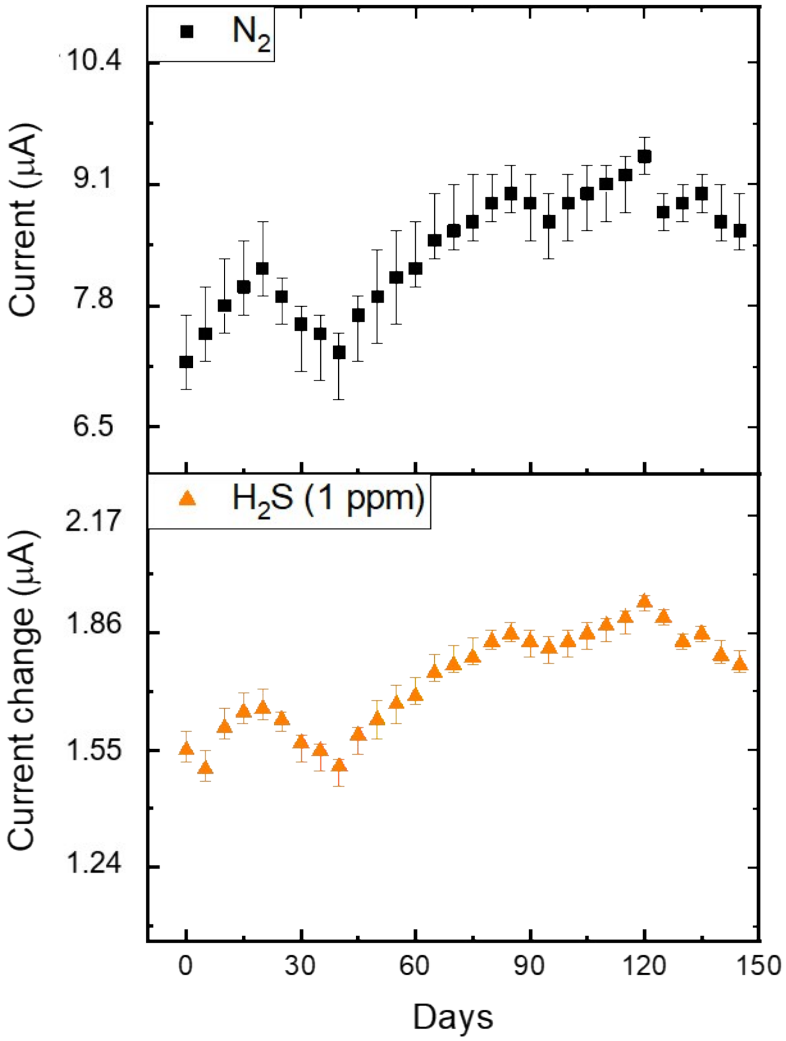

**Fig. S25 Ambient stability of D3 OFET sensor**. Stability of the D3 OFET device was monitored for a total of 150 days by recording the current response under (top) $N_2$ inert atmosphere and (bottom) $H_2S$ (1 ppm) gas for every 5 days.

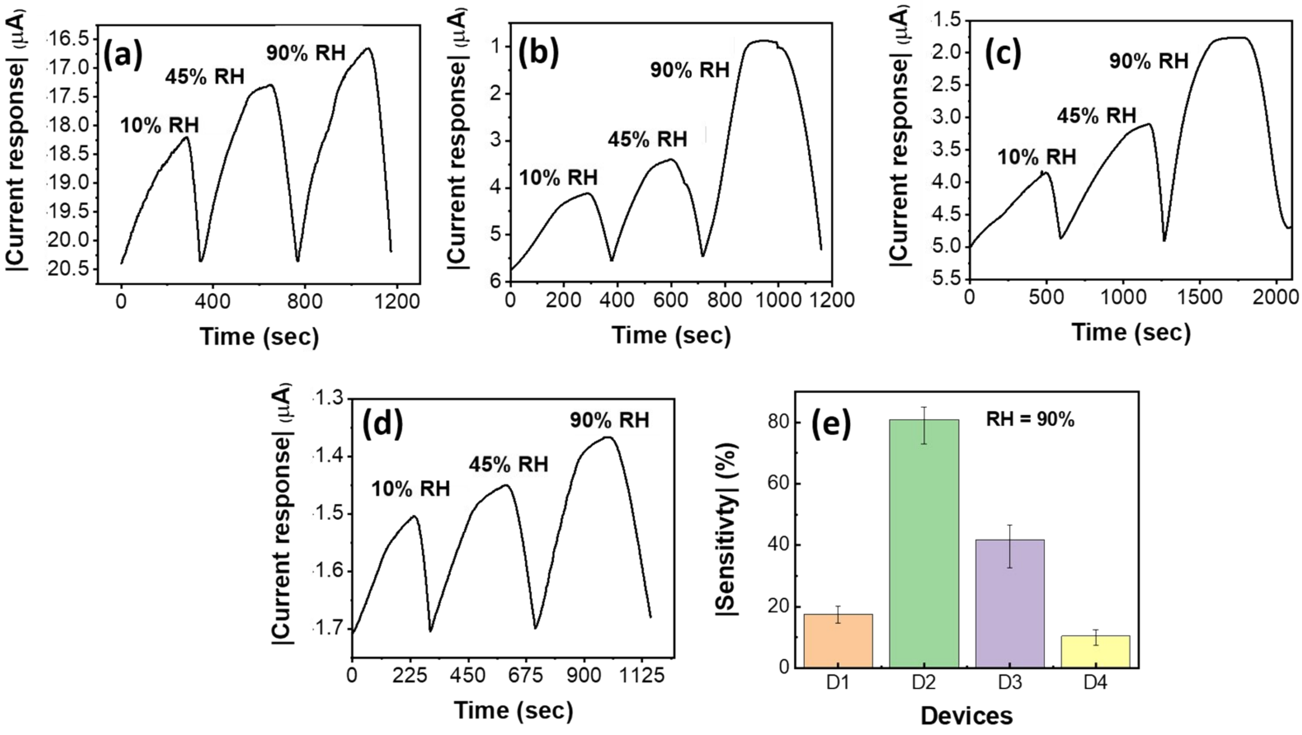

**Fig. S26 Moisture stability of the OFET devices**. Transient response of (a) D1, (b) D2, (c) D3 and (d) D4 OFET devices toward different Relative humidity (RH) conditions such as 10%, 45% and 90% RH.

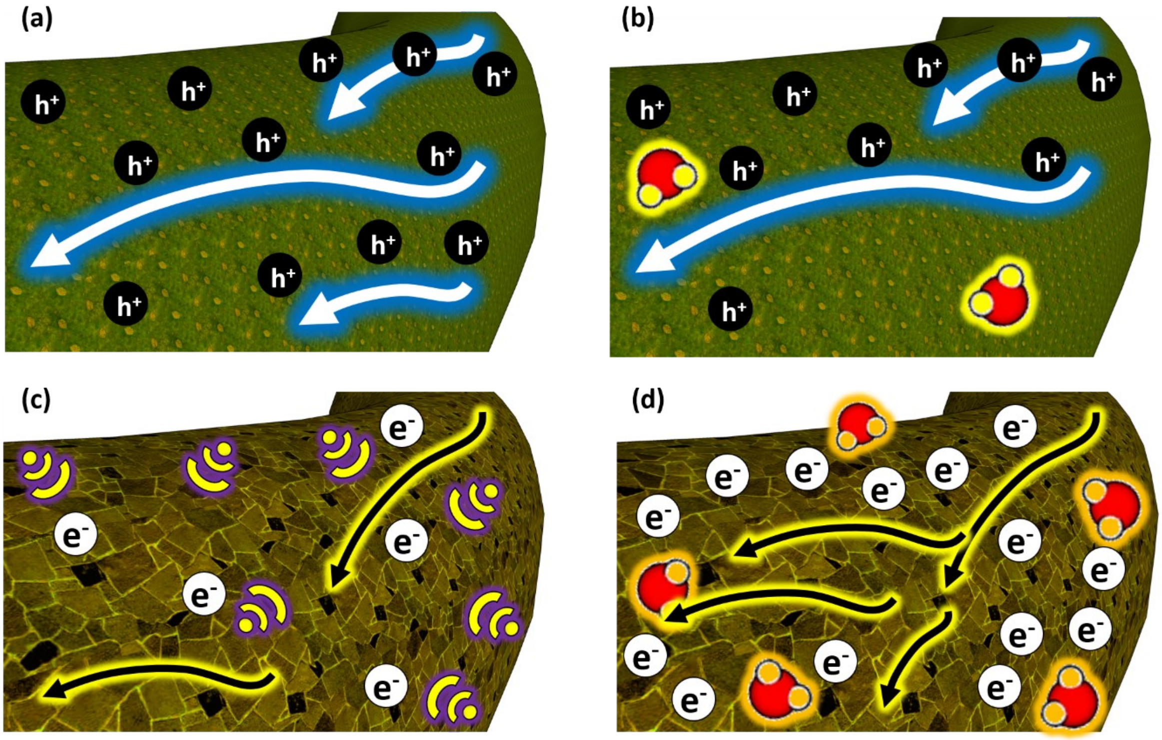

**Fig. S27** Schematic illustration of charge transport in (a) M1 material before H2S gas exposure, (b) M1 material after H2S gas exposure, (c) M4 material before H2S gas exposure and (d) M4 material after H2S gas exposure.

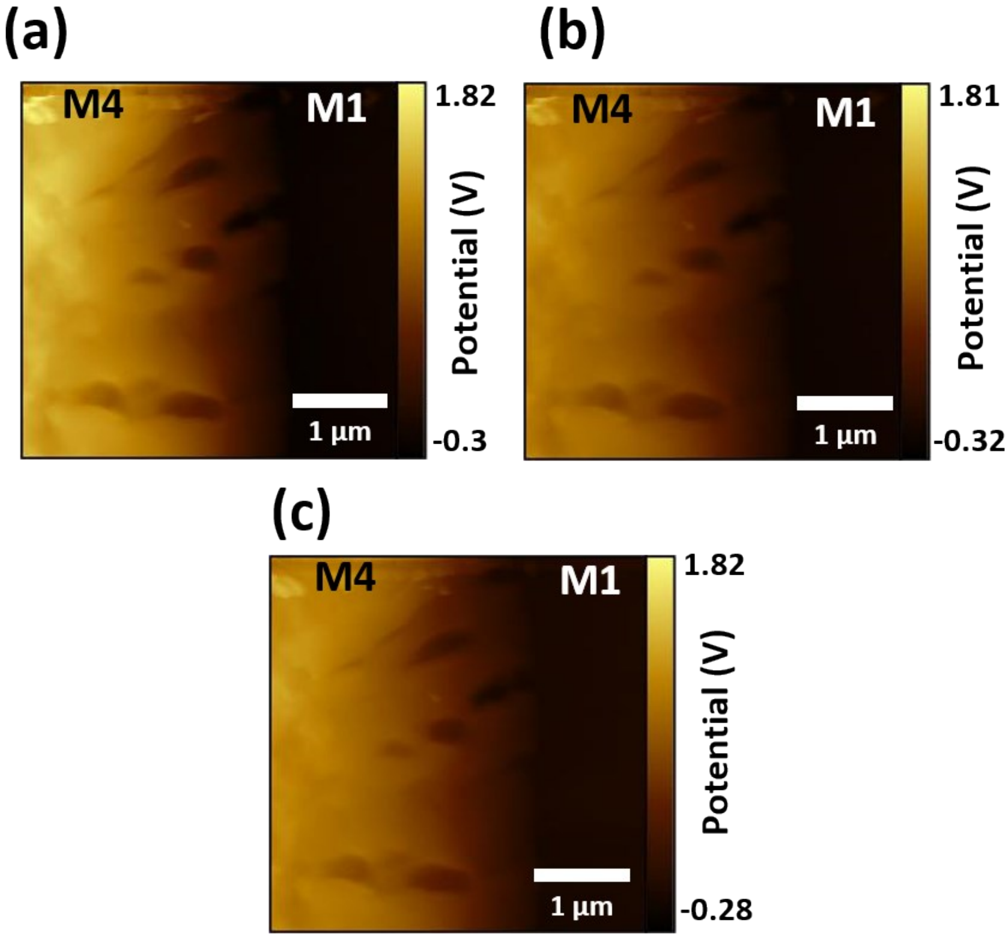

**Fig. S28 Surface KPFM characterization of the gas exposed absorbent materials**. Contact potential difference (CPD) map was recorded 30 min after exposing the M4 (left) and M1 (right) materials toward (a) $H_2S$, (b) $NH_3$ and (c) $NO_2$ analytes.

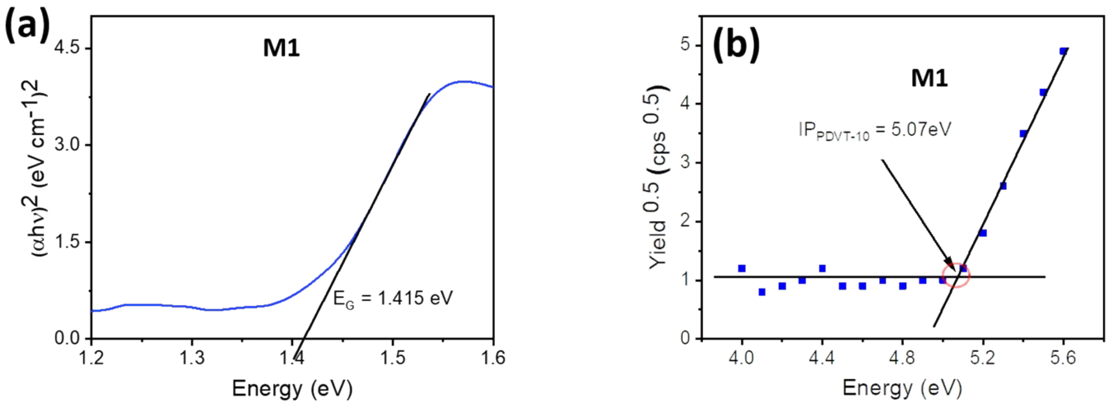

**Fig. S29 Optical characterization of M1 material**. (a) The optical bandgap is calculated from the Tauc plot spectrum, and (b) Ionization potential (IP) is extracted from the recorded Photoelectron spectroscopy in the air (PESA) spectrum

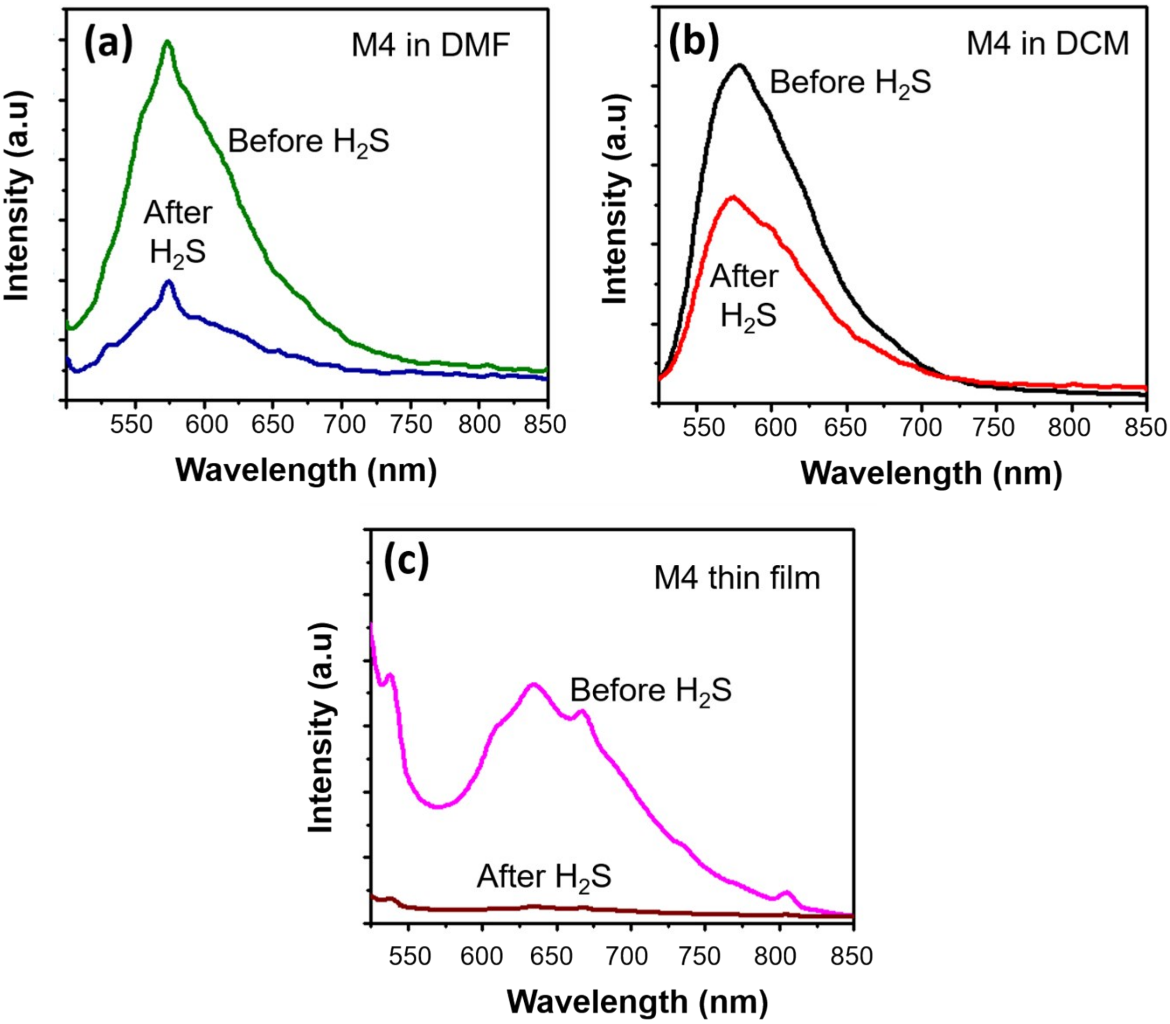

**Fig. S30 Photophysical characterization of M4 material.** Emission spectra of solutions of M4 material before and after exposure to $H_2S$ dissolved in two different solvents: (a) DMF and (b) DCM. (c) Emission spectra of a drop-casted thin-film of M4 material before and after exposure to $H_2S$

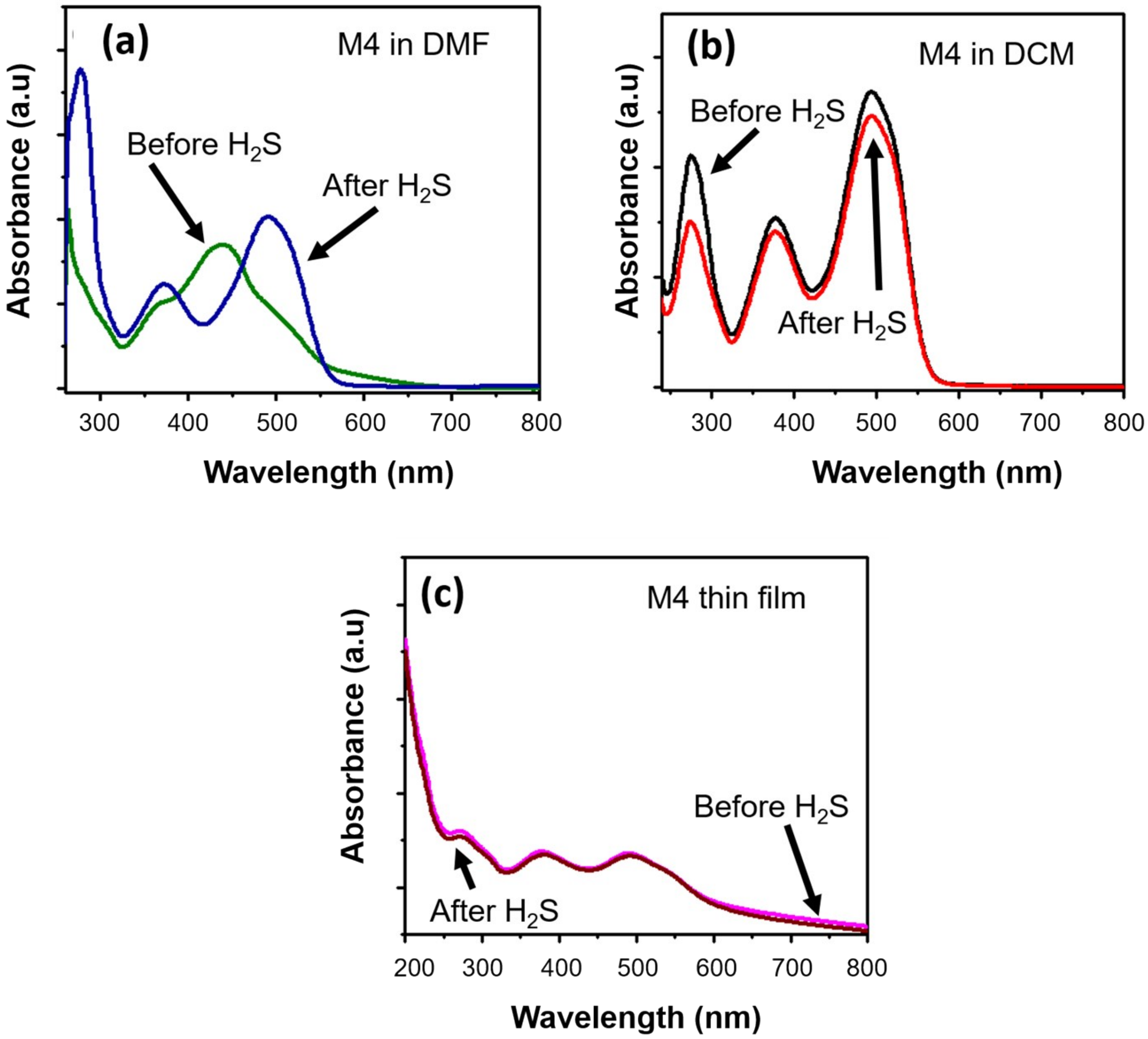

**Fig. S31 Optical characterization of M4 material**. UV-Vis spectra of solutions of M4 material before and after exposure to $H_2S$ dissolved in two different solvents: (a) DMF and (b) DCM. (c) Absorption spectra of a drop-casted thin-film of M4 material before and after exposure to $H_2S$

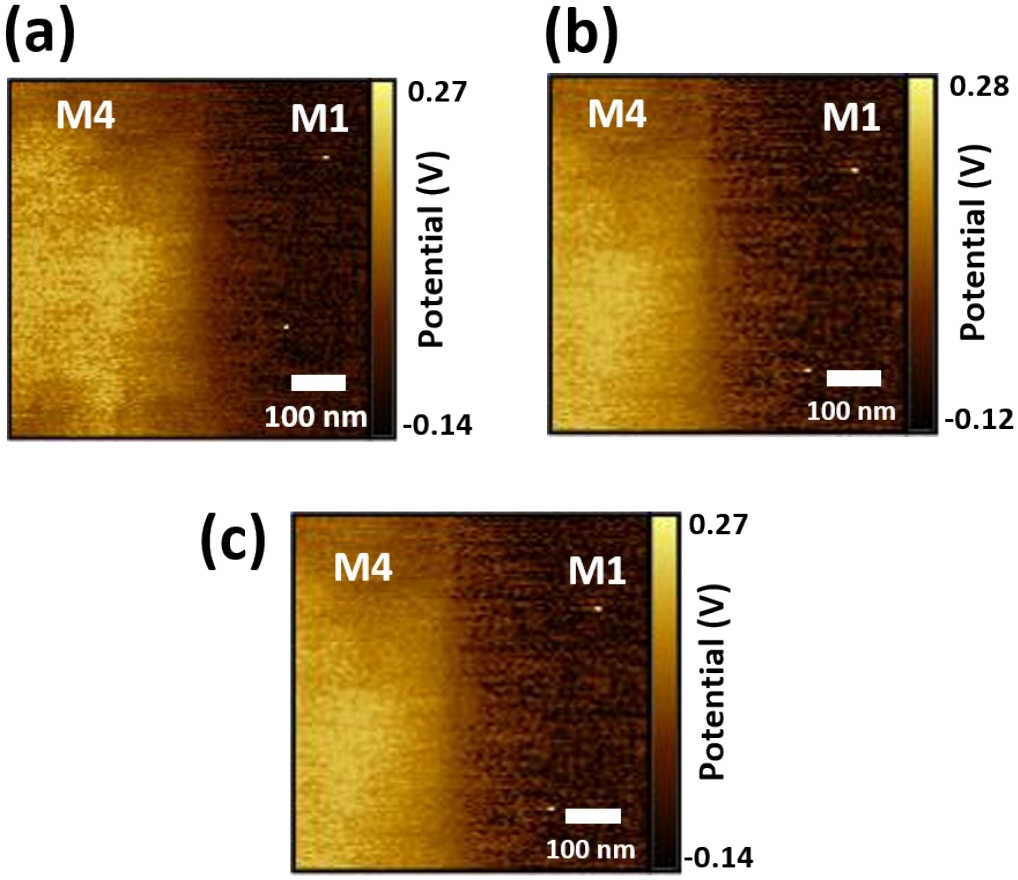

**Fig. S32 Cross-section KPFM characterization of the gas exposed absorbent materials**. Contact potential difference (CPD) potential map was recorded 30 minutes after exposing the M4 (left) and M1 (right) materials toward (a) $H_2S$, (b) $NH_3$ and (c) $NO_2$ analytes.

**Table S1. Thickness, roughness and CPD values of all the gas absorbent materials (M1-M4) are tabulated.**

| **Materials** | **M1** | **M2** | **M3** | **M4** |
|---|---|---|---|---|
| **Thickness (nm)** | 23.20 ± 5.70 | 168.50 ± 15.15 | 233.20 ± 20.20 | 235.00 ± 13.55 |
| **Roughness (nm)** | 0.95 ± 0.30 | 5.20 ± 0.55 | 3.70 ± 0.40 | 2.30 ± 0.75 |
| **CPD (V)** | -0.23 ± 0.15 | 1.00 ± 0.05 | 1.50 ± 0.11 | 1.85 ± 0.20 |

**Table S2. Transistor parameter values for all the fabricated OFET devices.**

| Devices | D1 | D2 | D3 | D4 |
|---|---|---|---|---|
| **Threshold voltage (V)** | -3.56 ± 0.75 | -8.5 ± 1.52 | -3.05 ± 1.21 | -1.51 ± 0.45 |
| **Current ration (x $10^4$)** | 3.24 ± 0.63 | 0.32 ± 0.21 | 1.76 ± 0.53 | 4.76 ± 1.05 |
| **Subthreshold swing (V/dec)** | 1.24 ± 0.45 | 3.25 ± 0.25 | 1.47 ± 0.43 | 1.24 ± 0.12 |
| **Transconductance (µS)** | 6.91 ± 0.61 | 0.23 ± 0.12 | 0.41 ± 0.05 | 3.24 ± 1.23 |
| **Mobility ($x10^{-2}$ $cm^2$ $V^{-1}$ $sec^{-1}$)** | 4.94 ± 0.23 | 0.32 ± 0.02 | 0.39 ± 0.11 | 1.24 ± 0.21 |

## Table S3. Room temperature operable $H_2S$ sensors work under conduction mechanism

| Group | Sensor materials | Sensitivity ($ppm^{-1}$) | LOD (ppm) | Testing range (ppm) | Stability studies |
|---|---|---|---|---|---|
| **Metal oxide** | ZnO nanowires[5] | 20% | 0.05 | 0.05 to 1 | Not performed |
| | CuO nanosheets[6] | 90% | 0.01 | 0.01 to 0.1;<br>1 to 60 | Ambient stability (30 days) |
| **Composite** | ZIF-8/ZnO[7] | 5.21% | 0.05 | 0.05 to 10 | Temperature effect (25 C to 300 C), Effect of humidity (0 – 90% RH), Ambient stability (9 weeks) |
| | Ag-In2O3 nanorods[8] | 300% | 0.005 | 0.005 to 20 | Effect of humidity (30% to 66% RH) and Ambient stability (15 days) |
| **2D materials** | MoSe2 nanoflakes[9] | 10% | 0.05 | 0.05 to 5 | Temperature effect (100 C to 300 C) and Ambient stability (1 month) |
| **Polymers** | Ph5T2[10] | 100% | 0.5 | 0.5 to 50 | Not performed |
| | Ph5T2 modified Copper thalocyanine (CuPC) nanowire[11] | 108% | 0.02 | 0.02 – 10 | NR |
| | Spirobiflourine based polymer[12] | 2.54% | 0.01 | 0.10 – 50 | Bias stress:<br>4 cycles under $N_2$ atmosphere |
| | PDPP4T-T-Hg(II)[13] | 60% | 0.005 | 0.005 to 0.1 | Not performed |
| | **PDVT-10/Tris(keto-hydrazone) (Our work)** | 545% | 0.001 | 0.005 to 25 | Effect of humidity (20 – 95% RH), Bias stress effect (10 hours) and Ambient stability (50 days) |

# References

[1] H. Y. Lee, X. Song, H. Park, M.-H. Baik, D. Lee, *Journal of the American Chemical Society* **2010**, 132, 12133.

[2] C. Li, J. Zhang, Z. Li, W. Zhang, M. S. Wong, G. Yu, *Journal of Materials Chemistry C* **2019**, 7, 297.

[3] a) B. Kim, S. I. Seok, *Energy & Environmental Science* **2020**, 13, 805; b) B. Kim, M. Kim, J. H. Lee, S. I. Seok, *Advanced Science* **2020**, 7, 1901840.

[4] X. Li, G. Baryshnikov, C. Deng, X. Bao, B. Wu, Y. Zhou, H. Ågren, L. Zhu, *Nature communications* **2019**, 10, 1.

[5] F. Huber, S. Riegert, M. Madel, K. Thonke, *Sensors and Actuators B: Chemical* **2017**, 239, 358.

[6] Z. Li, N. Wang, Z. Lin, J. Wang, W. Liu, K. Sun, Y. Q. Fu, Z. Wang, *ACS applied materials & interfaces* **2016**, 8, 20962.

[7] X. Wu, S. Xiong, Y. Gong, Y. Gong, W. Wu, Z. Mao, Q. Liu, S. Hu, X. Long, *Sensors and Actuators B: Chemical* **2019**, 292, 32.

[8] S. Yan, Z. Li, H. Li, Z. Wu, J. Wang, W. Shen, Y. Q. Fu, *Journal of Materials Science* **2018**, 53, 16331.

[9] R. K. Jha, J. V. D'Costa, N. Sakhuja, N. Bhat, *Sensors and Actuators B: Chemical* **2019**, 297, 126687.

[10] O. Yassine, O. Shekhah, A. H. Assen, Y. Belmabkhout, K. N. Salama, M. Eddaoudi, *Angewandte Chemie International Edition* **2016**, 55, 15879.

[11] Z. Song, G. Liu, Q. Tang, X. Zhao, Y. Tong, Y. Liu, *Organic Electronics* **2017**, 48, 68.

[12] A. Lv, M. Wang, Y. Wang, Z. Bo, L. Chi, *Chemistry–A European Journal* **2016**, 22, 3654.

[13] Y. Yang, Z. Liu, L. Chen, J. Yao, G. Lin, X. Zhang, G. Zhang, D. Zhang, *Chemistry of Materials* **2019**, 31, 1800.